RNase H1 facilitates recombinase recruitment by degrading DNA–RNA hybrids during meiosis

Chao Liu[1,6,†], **Liying Wang**[1,†], **Yanan Li** [2,†], **Mengmeng Guo**[6,9], **Jun Hu**[5], **Teng Wang**[2], **Mengjing Li**[4], **Zhuo Yang**[3], **Ruoyao Lin**[5], **Wei Xu** [3], **Yinghong Chen**[6,9], **Mengcheng Luo** [7], **Fei Gao** [6,9], **Jia-Yu Chen**[5], **Qianwen Sun** [3,8], **Hongbin Liu** [4], **Bo Sun** [2,*] **and Wei Li** [1,6,9,*]

[1]Guangzhou Women and Children's Medical Center, Guangzhou Medical University, Guangzhou 510623, China, [2]School of Life Science and Technology, ShanghaiTech University, Shanghai 201210, China, [3]Center for Plant Biology, School of Life Sciences, Tsinghua University, Beijing 100084, China, [4]Center for Reproductive Medicine, Shandong University, Jinan 250012, China, [5]State Key Laboratory of Pharmaceutical Biotechnology, School of Life Sciences, Chemistry and Biomedicine Innovation Center (ChemBIC), Nanjing University, Nanjing 210023, China, [6]State Key Laboratory of Stem Cell and Reproductive Biology, Institute of Zoology, Stem Cell and Regenerative Medicine Innovation Institute, Chinese Academy of Sciences, Beijing 100101, China, [7]Department of Tissue and Embryology, School of Basic Medical Sciences, Wuhan University,Hubei Provincial Key Laboratory of Developmentally Originated Disease, Wuhan 430072, China, [8]Tsinghua-Peking Center for Life Sciences, Beijing 100084, China and [9]University of Chinese Academy of Sciences, Beijing 100049, China

ABSTRACT

DNA–RNA hybrids play various roles in many physiological progresses, but how this chromatin structure is dynamically regulated during spermatogenesis remains largely unknown. Here, we show that germ cell-specific knockout of *Rnaseh1*, a specialized enzyme that degrades the RNA within DNA–RNA hybrids, impairs spermatogenesis and causes male infertility. Notably, *Rnaseh1* knockout results in incomplete DNA repair and meiotic prophase I arrest. These defects arise from the altered RAD51 and DMC1 recruitment in zygotene spermatocytes. Furthermore, single-molecule experiments show that RNase H1 promotes recombinase recruitment to DNA by degrading RNA within DNA–RNA hybrids and allows nucleoprotein filaments formation. Overall, we uncover a function of RNase H1 in meiotic recombination, during which it processes DNA–RNA hybrids and facilitates recombinase recruitment.

GRAPHICAL ABSTRACT
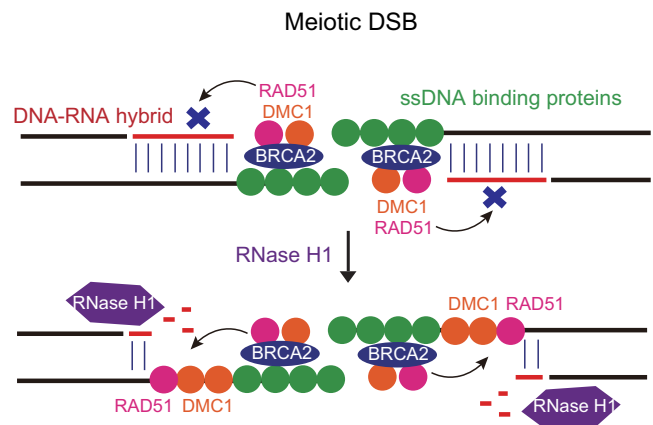
INTRODUCTION

A DNA–RNA hybrid is a specific chromatin structure formed by RNA annealing with template DNA strands (1,2). DNA–RNA hybrids are formed during gene transcription, DNA replication, and DNA repair processes (1–3). Homeostasis emerges with the constant formation and removal of DNA–RNA hybrids throughout the genome, and it plays important roles in various biological processes, such as gene expression, chromatin remodeling, DNA replication, and genomic stability across many organisms (1–6). Many regulators, such as RNA N6-methyladenosine,

topoisomerases, DNA–RNA hybrid helicases, and RNase H endonucleases, have been reported to participate in the maintenance of DNA–RNA hybrid homeostasis (1,7,8). Ribonuclease H1 (RNase H1) is a specialized enzyme that degrades the RNA within DNA–RNA hybrids (9,10). Although an understanding about RNase H1's functions has been rapidly accumulating in recent years, its functional roles in many physiological processes remain unknown.

Spermatogenesis is a specialized cellular differentiation process for male gamete production, whereby spermatogonial stem cells (SSCs) undergo mitosis, meiosis, and spermiogenesis (11,12). During spermatogenesis, SSCs undergo proliferation and differentiate into spermatocytes, which perform a single round of DNA replication followed by two consecutive cell divisions, termed meiosis, to generate haploid germ cells (13,14). Then, the haploid germ cells undergo a dramatic morphological change and chromatin compaction to produce matured spermatozoa, which are subsequently matured in the epididymis (14,15). Many factors and regulatory mechanisms have been identified to modulate spermatogenesis, and the deficiency of spermatogenesis often results in spermatogenic failure and causes male infertility (16). As a specific chromatin structure, the DNA–RNA hybrid has also been hinted to be involved in spermatogenesis. In the *C. elegan* germline, accumulated DNA–RNA hybrids have been shown to induce irreparable DSBs that evade DNA damage checkpoints and drive germline mutagenesis (17). In mice, the knockout of Senataxin, a DNA–RNA hybrid helicase, causes the accumulation of DNA–RNA hybrids in spermatocytes, which impairs meiotic sex chromosome inactivation (MSCI) (18,19). In addition, some ataxia patients with *SETX* mutations showed perturbed spermatogenesis and male infertility (20,21). However, the relationship between DNA–RNA hybrid regulators and male infertility and their potential function(s) in spermatogenesis is still far from well understood.

To address the above questions, we specifically knocked out *Rnaseh1* in germ cells by crossing *Rnaseh1^{Flox/Flox}* mice with *Stra8-GFPCre* transgenic mice and found that the knockout of *Rnaseh1* severely impaired spermatogenesis and caused male infertility. Further immunofluorescence analysis shows that the knockout of *Rnaseh1* impairs the recruitment of RAD51 and DMC1 to DSB sites in zygotene spermatocytes, resulting in incomplete DNA repair and impaired crossover formation and meiotic prophase I arrest. Particularly, the generation of DNA–RNA hybrids during meiosis is highly associated with meiotic DSB formation, and germ cell-specific *Rnaseh1* knockout causes a severe accumulation of DNA–RNA hybrids in meiosis prophase I, indicating that recombinases fail to load onto DNA–RNA hybrids. Furthermore, single-molecule experiments demonstrate that DNA–RNA hybrids significantly suppress the recruitment of RAD51 and DMC1. In stark contrast, the presence of RNase H1 facilitates RNA removal and thereby allows RAD51 and DMC1 nucleoprotein filaments formation. Taken together, we reveal that the DNA–RNA hybrids are dynamically regulated during spermatogenesis, and RNase H1 degrades the hybrids to facilitate RAD51 and DMC1 recruitment during meiotic recombination.

MATERIALS AND METHODS

Animals

The *Stra8-GFPCre* knock-in mouse line was kindly gifted by Dr Ming-Han Tong (Chinese Academy of Sciences Center for Excellence in Molecular Cell Science) (22). The *Rnaseh1* Floxed mouse was generated using CRISPR/Cas9 system. Briefly, the T7 promoter and guiding sequences targeted for *Rnaseh1* exon 4 were added to the sgRNA by PCR amplification using the following primers: *Rnaseh1-Floxed*-usgRNA1: TAA TAC GAC TCA CTA TAG AGA GGA GGG GCC AGG CAC GGT TTA AGA GCT ATG CTG GAA AC;*Rnaseh1-Floxed*-usgRNA2: TAA TAC GAC TCA CTA TAG TAT AAG CAG GTC TCC TAG TGT TTA AGA GCT ATG CTG GAA AC;*Rnaseh1-Floxed*-dsgRNA1: TAA TAC GAC TCA CTA TAG CTG GGT CTG TAT AAG TAC TAG TTT AAG AGC TAT GCT GGA AAC; *Rnaseh1-Floxed*-dsgRNA2: TAA TAC GAC TCA CTA TAG CCA GCC AGC AGC GAT GCG GGT TTA AGA GCT ATG CTG GAA AC. *Rnaseh1-Floxed*-usgRNA1 and *Rnaseh1-Floxed*-usgRNA2 were used for inserting the upstream *LoxP* site, *Rnaseh1-Floxed*-dsgRNA1 and *Rnaseh1-Floxed*-dsgRNA2 were used for inserting the downstream *LoxP* site. In the *Rnaseh1*-targeting construct, a 5.0-kb genomic DNA segment harboring exon 4 was flanked by *LoxP* sites (Supplementary Figure S1). The B6D2F1 (C57BL/6 × DBA2) and ICR female mice were used as embryo donors and foster mothers, respectively. The fertilized embryos were collected from the oviducts of B6D2F1 female mice mated with B6D2F1 stud males. Cas9 mRNA (10 ng), sgRNA (5ng), and donor DNA (10ng) were injected into the cytoplasm of fertilized eggs with well-recognized pronuclei in M2 medium (Sigma, M7167). The injected zygotes were cultured in KSOM (modified simplex-optimized medium, Millipore) with amino acids at 37°C with 5% CO_2, and about 15–25 blastocysts were transferred into the uterus of pseudopregnant ICR female mice. To construct germ cell-specific *Rnaseh1* knockout mice, *Rnaseh1*-floxed mice were bred with the *Stra8-GFPCre* mouse line to excise *LoxP*-flanked exons 4, thus generating *Rnaseh1*-conditional knockout mice. Genotyping PCR for *Rnaseh1* was performed using the following primers: *Rnaseh1*-forward-1: AGA CCA CTC GCC AGC AAA TTG GCT, *Rnaseh1*-reverse-1: GCA CCG ACC TGC TCA ACA GTG ACC ACT; *Rnaseh1*-forward-2: TTG CTA AAC TGC TAG GTA AAC AGT GTT GGC TGG GA, *Rnaseh1*-reverse-2: GGT TCA GTT TTA CAC CTT TGC CTG TGT TCT CTG ACT. The PCR conditions were as follows: 94°C for 5 min; 35 rounds of 94°C for 30 s, 65°C for 30 s, and 72°C for 1 min; and 72°C for 5 min. The *Spo11* and *Dmc1* knockout mice have been described previously (23). All of the animal experiments were performed according to approved institutional animal care and use committee (IACUC) protocols (#08–133) of the Institute of Zoology, Chinese Academy of Sciences.

Antibodies

Mouse antibodies to γH2AX (05-636) and mouse antibody to ATMps1981 (05-740) were purchased from Merck Millipore (Darmstadt, Germany). Mouse antibodies to

MLH1 (51-1327GR) were purchased from BD Pharmingen (San Diego, USA). Rabbit antibodies against SYCP3 (150292), BRCA2 (ab123491), RPA2 (ab76420), RAD51 (ab133534), NBS1 (ab32074) were purchased from Abcam (Cambridge, USA). Rabbit antibody to MRE11 (NB100-142) was purchased from Novus Biologicals (Littleton, USA). Mouse antibody to SYCP3 (SC-74569), rabbit antibody to DMC1 (SC-22768) were purchased from Santa Cruz Biotechnology (Dallas, USA). Rabbit antibody to RNase H1 (DF12084) for immunofluorescence was purchased from Affinity Biosciences (Jiangsu, China). Rabbit antibodies to RNase H1 (15606-1-AP), SPATA22 (16989-1-AP), HSP60 (15282-1-AP), TOM20 (11802-1-AP), HOP2 (11339-1-AP) were purchased from Proteintech (Rosemont, USA). Goat antibody to c-KIT (AF1356) was purchased from R&D Systems (Minneapolis, USA). Rabbit antibodies to Tubulin (AC007) and GAPDH (AC001) were purchased from Abclonal (Wuhan, China). Mouse anti-DNA–RNA hybrid [S9.6] antibody (ENH001) was purchased from Kerafast (Boston, USA). Rabbit antibody to MEIOB was obtained as previously described (24). Rabbit anti-HEI10 polyclonal antibody was generated by Dai-an Biological Technology Incorporation (Wuhan, China). Goat anti-rabbit FITC (ZF-0311), goat anti-mouse FITC (ZF-0312), and goat anti-mouse TRITC (ZF-0313)-conjugated secondary antibodies were purchased from Zhong Shan Jin Qiao (Beijing, China). Alexa Fluor 680-conjugated goat anti-rabbit (A21109) antibodies for immunoblotting were purchased from Invitrogen (Carlsbad, USA).

Assessment of the fertility of *stra8-rnaseh1*$^{-/-}$ mice

The fertility assessment experiments were performed as previously described (25). A male mouse was caged with two wild-type female mice, and their vaginal plugs were checked every morning. The plugged females were separated and caged individually, and the pregnancy outcomes were recorded. Females that did not generate offspring at 22 days post conception were scored as not being pregnant and euthanized.

Tissue collection and histological analysis

Mouse testis and cauda epididymis were immediately dissected after euthanasia, fixed in Bouin's solution (Picric acid:methanol:acetic acid = 15:5:1) or 4% (mass/vol) paraformaldehyde (PFA; Solarbio, China, P1110) for 24 h. The tissues were then dehydrated and embedded in paraffin. 5 μm tissue sections were collected and mounted on glass slides for further processing. After deparaffinization, tissue sections were stained with hematoxylin-eosin (H&E) for histological analysis and periodic acid-Schiff (PAS)-hematoxylin for determining the seminiferous epithelia cycle stages according to the method described previously (26).

Epididymal sperm count

The caudal epididymis was dissected immediately after euthanasia. Spermatozoa were squeezed out from the caudal epididymis and incubated in PBS for 30 min at 37°C under 5% CO_2. The incubated sperm medium was then diluted at 1:100 and transferred to a hemocytometer for counting.

Immunoblotting

Testis proteins were extracted in RIPA-like lysis buffer (25 mM Tris–HCl, pH 7.6, 500 mM NaCl, 2 mM EDTA, 1% sodium deoxycholate, 0.1% SDS) plus a protein inhibitor mixture (Roche, 04693132001). After testis grinding and ultrasonication, the samples were incubated on ice for 30 min. The protein lysates were then centrifuged at 13 500 g for 15 min at 4°C. The supernatants of the extracts were used for immunoblotting. Protein samples were separated via SDS-PAGE and transferred to a nitrocellulose membrane by a semi-dry transfer method. After incubation with primary and secondary antibodies, the membrane was scanned using an ODYSSEY Sa Infrared Imaging System (LI-COR Biosciences, USA).

Immunofluorescence

The spermatocytes were spread on glass slides as previously described (27). Spermatocyte chromosomal spreads were washed with PBS three times and blocked with 5% bovine serum albumin (BSA, Amresco, USA, AP0027). The primary antibody was added to the sections and incubated at 4°C overnight, followed by incubation with the secondary antibody. The nuclei were stained with 4′,6-diamidino-2-phenylindole (DAPI). The immunofluorescence images were taken immediately using an LSM 780 microscope (Zeiss, Germany) or SP8 microscope (Leica, Germany). TUNEL assays were carried out using the In Situ Cell Death Detection Kit (Roche Diagnostics, 11684795910, Switzerland) according to the manufacturer's instructions (28).

DNA extraction and mtDNA quantification

Genomic DNA from mouse testis was isolated after SDS/proteinase K treatment at 37°C overnight. DNA was extracted using a phenol/chloroform method and precipitated with isopropanol. The mtDNA copy number was measured by qPCR in a QuantStudio 6 Flex Real-Time PCR System, following the protocol of the manufacturer (29). The mt DNA primer probes were previously described (30,31) and listed in Supplementary Table S1. The HK2 probe was used to normalize samples to the nuclear DNA content.

Super-resolution imaging

Super-resolved images were acquired using a Zeiss Elyra S.1 3D-SIM system, as previously described (32). Briefly, hundred nanometers-thick Z Sections were acquired in 3D SIM mode generating 7 images per plane (5 phases, 3 angles) as a raw image, which was reconstructed to generate a super-resolution image. Channel alignment was conducted using calibrated file generated from 200 nm diameter tetraspectral fluorescent spheres (Life technologies). Acquired images were processed with structured illumination and further adjusted by channel alignment methods in ZEN 2.3 SP1 software.

Isolation of mouse spermatogenic cells

Spermatogenic cells were isolated using a method previously described with a slight modification (27). Briefly, testes were dissected and decapsulated immediately after euthanasia. The seminiferous tubules were cut into small pieces and incubated in PBS containing 1 mg/ml collagenase (Sigma, C5138) and 1 mg/ml hyaluronidase (Sigma, H3506) at 37°C for 6 min with gentle shaking. After pipetting, the dispersed seminiferous tubules and cells were incubated at 37°C for 5 min with gentle shaking. Then, the cells were collected by centrifugation at $200 \times g$ for 5 min at 4°C, washed once with PBS, resuspended in PBS containing 0.25% Trypsin and 1 mg/ml DNase I, and incubated at 37°C for 5 min with gentle shaking. Thereafter, the cells were collected by centrifugation at $200 \times g$ for 5 min at 4°C and washed with PBS. After filtration through a 40 μm Nylon Cell Strainer (BD Falcon, 352340), the cells were separated by sedimentation velocity at unit gravity at 4°C, using a 2–4% BSA gradient. An aliquot of each fraction was examined by light microscope to assess cellular purity and cell type identity. The fractions containing the expected cell type (Sertoli cells, spermatocytes, round spermatids, elongated spermatids) and purity were pooled together.

Protein expression and purification

Rad51-af555. The human RAD51 open reading frame was subcloned between the NcoI and BamHI sites of pET11d (Novagen). The cysteine-to-serine variants were generated by the QuikChange site-directed mutagenesis method by using the WT RAD51 pET11d subclone as a template. The expression plasmid was transformed into BL21 (DE3). This strain was then cultured and induced by 1 mM isopropyl-1-thio-D-galactopyranoside (IPTG) at 18°C for 16 h. The protein was purified using a heparin Sepharose column. To fluorescently label RAD51, the DTT concentration was adjusted to 20 mM in the purified RAD51 samples (at 1 - 2 mg/ml of RAD51) and incubated for 30 min on ice. The sample was buffer-exchanged into labeling buffer containing 50 mM MOPS–HCl (pH 7.0), 300 mM KCl, 1 mM EDTA, 10% glycerol, and degassed with argon for 30 min before use. The maleimide-coupled Alexa Fluor 555 dye (Molecular Probes) was resuspended in labeling buffer and immediately added to the protein sample at a 10-fold molar excess. The reaction was incubated on ice for 30 min and quenched by adding DTT to 20 mM with a further 30 min incubation on ice. Excess dyes were removed by buffer exchange into 0.3 M KCl, 50 mM Tris–HCl (pH 7.5), 1 mM EDTA, 2 mM DTT, and 10% glycerol (33,34).

DMC1-eGFP. The human DMC1 gene and eGFP gene were constructed into pET28a by using NdeI and NotI restriction sites (Tsingke Biotechnology). In the resulting plasmid, named pET28a-DMC1-eGFP, the N and C terminus of DMC1 were fused to a His6-tag and an eGFP, respectively. The protein purification was modified from a previously described procedure (35,36). The expression plasmid was transformed into BL21 (DE3). This strain was then cultured and induced by 1 mM isopropyl-1-thio-D-galactopyranoside (IPTG) at 18°C for 16 h. Cells were collected by centrifugation and resuspended in lysis buffer containing 25 mM Tris–HCl (pH 7.5), 300 mM KCl, 10 mM imidazole, 10% glycerol and 1 mM phenylmethylsulfonyl fluoride and passed through a homogenizer three times at ∼850 bar. The lysed dilution was then ultracentrifuged at 11 000 g for 30 min. The supernatant was applied to a Ni-Sepharose resin, washed extensively with 25 mM Tris–HCl (pH 7.5), 300 mM KCl, 50 mM imidazole and 10% glycerol, and then the bound protein was eluted in a single step with elution buffer containing 25 mM Tris–HCl (pH 7.5), 300 mM KCl, 300 mM imidazole and 10% glycerol. Finally, the protein sample was buffer-exchanged into the storage buffer containing 25 mM Tris–HCl (pH 7.5), 300 mM KCl, and 10% glycerol and stored at −80°C before use.

RNase H1. The human RNase H1 was purchased from Abmart (Product No: EHH9801).

Preparation of DNA–RNA hybrid templates

The detailed procedures to construct the DNA–RNA hybrid template used in the single-molecule assay were described previously (37). Briefly, the 7.4-kb DNA–RNA hybrid template consists of two pieces of single-stranded nucleic acids: a two-side biotinylated 7.4-knt ssDNA and a 7.4-knt ssRNA. A 7.4-kb dsDNA segment was PCR-amplified from the lambda DNA (Thermo). Using this dsDNA and a biotin-labeled primer, the second asymmetric PCR was carried out to produce the ssDNA. The resulting dsDNA and ssDNA were separated by agarose gel electrophoresis, and GeneJET Gel Extraction Kit (Thermo) was used for ssDNA purification. The 3′-end biotin labeling of the ssDNA was made by using biotinylated dATP (APExBIO) with terminal transferase. To construct the ssRNA, a 7.4-kb dsDNA including a T7 promoter (T7 DNA) at the 5′ end was PCR-amplified from λ phage DNA. The 7.4-knt ssRNA was generated by transcribing from the T7 DNA. The DNA–RNA hybrids were formed by annealing the two single-stranded nucleic acids in TE buffer.

Single-molecule optical tweezer assay and data analysis

Single-molecule optical tweezer assays were performed at 25°C on an instrument combining three-color confocal fluorescence microscopy with dual optical traps (LUMICKS C-trap, Netherland) (38,39). In the single-molecule assay, a DNA–RNA hybrid molecule was first captured between two streptavidin-coated polystyrene beads (1.76 μm in diameter, Spherotech). The DNA–RNA hybrid tether was then moved to protein channels as described for each assay. Experiments involving RNase H1, RAD51-AF555, or DMC1-eGFP were conducted in reaction buffer containing 25 mM Tris–HCl (pH 7.5), 150 mM KCl, 5 mM $MnCl_2$, 0.05 mg/ml BSA, 2 mM ATP and 1 mM DTT. A 488-nm excitation laser was used for imaging DMC1-eGFP, and a 532-nm excitation laser was used for imaging RAD51-AF555. The confocal pixel size was set to 50 nm. The pixel dwell time was 1 ms.

Single-molecule data were analyzed using custom software provided by LUMICKS. Pseudocolor was applied in ZEN 3.2 software (Zeiss) for better visualization of the signal contrast. Images were analyzed using Fiji. For the fluorescence signal, the total pixel intensities of the DNA–RNA

hybrid or ssDNA region in each frame were summed up using Fiji.

Statistical analysis

All data are presented as the mean ± SEM or ± SD. The statistical significance of the differences between the mean values for the different genotypes was measured by Student's *t*-tests with a paired, two-tailed distribution. The data were considered significant when the *P*-value was less than 0.05 (*), 0.01 (**) or 0.001 (***).

RESULTS

Germ cell-specific knockout of *rnaseh1* causes male infertility

Ribonuclease H1 (RNase H1) is a key modulator for DNA–RNA hybrid homeostasis by degrading RNA within DNA–RNA hybrids (9). Given that the conventional knockout of *Rnaseh1* causes embryonic lethality by impairing mitochondrial DNA (mtDNA) replication (40), we generated a conditional knockout allele of *Rnaseh1* by flanking exon 4 with loxP sites (Figures 1A, B) to explore the potential role of RNase H1 in spermatogenesis. *Rnaseh1* was specifically knocked out in germ cells by crossing mice with the Floxed *Rnaseh1* allele to *Stra8-GFPCre* mice, which express Cre recombinase from type A1 spermatogonia (Figure 1A) (22). Hereafter, germ cell-specific *Rnaseh1* knockout mice were referred to as *Stra8-Rnaseh1$^{-/-}$*. To detect the *Rnaseh1* knockout efficiency, the total protein extracted from *Rnaseh1$^{Flox/Flox}$* (hereafter referred to as *Rnaseh1$^{F/F}$*) and *Stra8-Rnaseh1$^{-/-}$* testes were utilized to perform the immunoblotting analysis of RNase H1. We found that the RNase H1 protein level was significantly reduced in *Stra8-Rnaseh1$^{-/-}$* testes compared with that in *Rnaseh1$^{F/F}$* testes (Figures 1C, D), indicating high knockout efficiency in *Stra8-Rnaseh1$^{-/-}$* mice. The residual protein signals of RNase H1 in *Stra8-Rnaseh1$^{-/-}$* testis may be due to the incomplete Cre recombinase activity (41) or the retained RNase H1 expressed in other cell types in mouse testis. Next, we assessed the effects of *Rnaseh1* knockout on male fertility. As shown in Figure 1E and 1F, no female mice became pregnant after mating with *Stra8-Rnaseh1$^{-/-}$* male mice, and *Stra8-Rnaseh1$^{-/-}$* male mice failed to produce any offspring (Figures 1E, F). Thus, germ cell-specific knockout of *Rnaseh1* results in male infertility.

RNase H1 is required for meiotic prophase completion during spermatogenesis

To further address how knockout of *Rnaseh1* influences male fertility, we then examined *Stra8-Rnaseh1$^{-/-}$* testis at gross and histological levels. We found that the size and weight of testes in *Stra8-Rnaseh1$^{-/-}$* mice were significantly reduced compared with that of *Rnaseh1$^{F/F}$* mice (Figures 1G, H). Hematoxylin-eosin (H&E) staining indicated that the structure of the seminiferous tubules in *Stra8-Rnaseh1$^{-/-}$* testis was disrupted, and large vacuoles and degenerated cells with highly condensed nuclei were observed in *Stra8-Rnaseh1$^{-/-}$* seminiferous epithelium (Figure 1I). Moreover, no spermatozoa could be detected in the cauda epididymis of *Stra8-Rnaseh1$^{-/-}$* mice (Figure 1I), and the

total number of spermatozoa in the *Stra8-Rnaseh1$^{-/-}$* mice significantly decreased compared with that of *Rnaseh1$^{F/F}$* mice (Figure 1J). These findings reveal that the knockout of *Rnaseh1* severely impairs spermatogenesis.

RNase H1 is required for mtDNA replication (29,40), and mitochondrial abundance increases during spermatogonia differentiation (42). Given that *Stra8-GFPCre* mice could express Cre recombinase from type A1 spermatogonia (22), we first examined the effect of *Rnaseh1* knockout on spermatogonia mtDNA replication. We found that the levels of both mtDNA and mitochondrial proteins, HSP60 and TOM20, did not decrease in *Stra8-Rnaseh1$^{-/-}$* testis compared with those of *Rnaseh1$^{F/F}$* testis (Supplementary Figure S1A–H). The immunofluorescence analysis also showed that the signal of TOM20 in *Stra8-Rnaseh1$^{-/-}$* type A spermatogonia (c-Kit positive cells) was similar to that of the control group (Supplementary Figure S1I). Furthermore, TUNEL-positive signals were not observed in *Stra8-Rnaseh1$^{-/-}$* type A spermatogonia (Supplementary Figure S1J). Given that Cre recombinase does not inactivate the floxed target gene in all mitotic germ cells (41), the subpopulation of type A spermatogonia harbouring active floxed alleles may be responsible for the observed results. Pursuing this, we examined the expression of RNase H1 in postnatal day 6 (PD6) testis, when Cre recombinase is highly expressed (41,43), and found that RNase H1 could still be detected in PD6 *Stra8-Rnaseh1$^{-/-}$* testis (Supplementary Figure S2A). In addition, we found that the RNase H1 is mainly expressed in spermatocytes and shows a lower expression level in type A spermatogonia (Supplementary Figure S2B), indicating that the little effect of *Rnaseh1* knockout on spermatogonia mtDNA replication might also be due to the low expression of RNase H1 in type A spermatogonia.

Next, we used Periodic Acid Schiff (PAS) and hematoxylin staining to examine testis sections and determine which stage of spermatogenesis was affected after *Rnaseh1* knockout. Multiple defects have been observed during *Stra8-Rnaseh1$^{-/-}$* spermatogenesis, and we detected dead preleptotene and pachytene spermatocytes at stage IV and stage VIII in our mice (Figure 2A). Those spermatocytes that did survive, died at stage XII as dead diplotene spermatocytes with some dead metaphase spermatocytes were observed at stage XII in *Stra8-Rnaseh1$^{-/-}$* seminiferous tubules (Figure 2A). The first wave of spermatogenesis is relatively synchronized (26), with the appearance of leptotene and zygotene spermatocytes at PD12 and pachytene spermatocytes at PD16 (44). We examined prepubertal testis sections by using H&E staining and found that the structure of the seminiferous tubules from *Stra8-Rnaseh1$^{-/-}$* mice in PD12 was similar to that of the control groups, whereas dead cells were detected in *Stra8-Rnaseh1$^{-/-}$* testis after PD17 (Supplementary Figure S3). Furthermore, TUNEL-positive signals were detected in the preleptotene, pachytene, diplotene, and metaphase spermatocytes at stages IV, VII, and XII in *Stra8-Rnaseh1$^{-/-}$* testes, but not in *Rnaseh1$^{F/F}$* testes (Figures 2B–D, Supplementary Figures S4A, B). Elevated DNA damage signals were detectable in *Stra8-Rnaseh1$^{-/-}$* preleptotene spermatocytes (Supplementary Figure S4C). These results suggest that germ cell-specific knockout of *Rnaseh1* impairs the
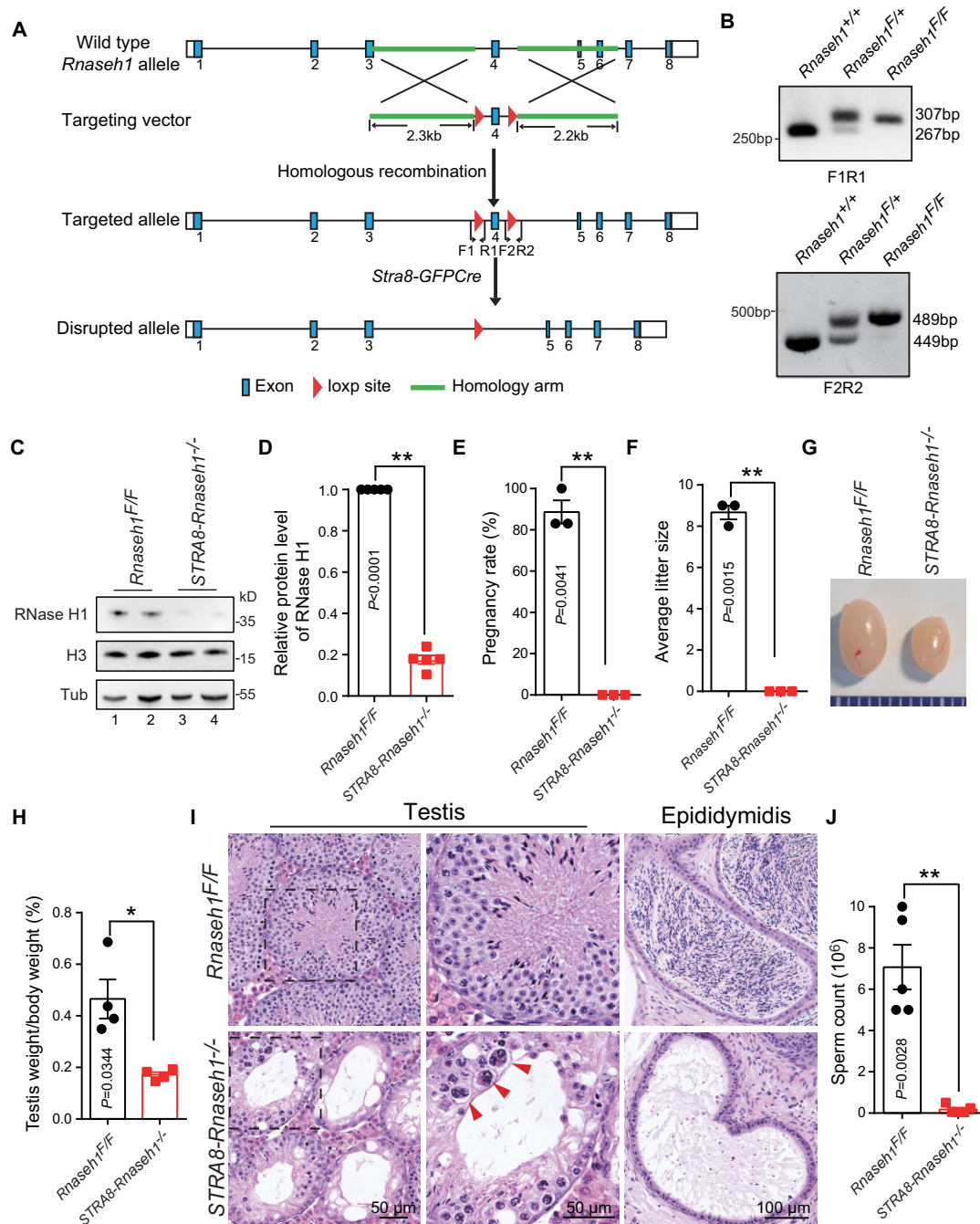
Figure 1. Germ cell-specific *Rnaseh1* knockout impairs mouse spermatogenesis and causes male infertility. (**A**) Schematic diagram for the construction of the *Rnaseh1^{F/F}* and *Stra8-Rnaseh1^{-/-}* mice. The mouse *Rnaseh1* locus surrounding exons 2, 3 and 4 is shown in the wild-type allele panel. (**B**) The geno-typing of the *Rnaseh1^{+/+}*, *Rnaseh1^{F/+}*, and *Rnaseh1^{F/F}* mice. (**C**) The RNase H1 protein levels are decreased in *Stra8-Rnaseh1^{-/-}* testes. Immunoblotting of RNase H1 is performed in *Rnaseh1^{F/F}* and *Stra8-Rnaseh1^{-/-}* testes. H3 and Tubulin serves as the loading control. (**D**) The quantification of RNase H1 protein levels in (C) (*n* = 5 independent experiments). Black dots indicate *Rnaseh1^{F/F}* mice, and red dots indicate *Stra8-Rnaseh1^{-/-}* mice. Data are presented as means ± SEM. two-tailed Student's *t*-test; **$P < 0.01$. (**E and F**) Germ cell-specific knockout of *Rnaseh1* causes male infertility. The fertility assessment experiments are performed in *Rnaseh1^{F/F}* and *Stra8-Rnaseh1^{-/-}* male mice. Pregnancy rates (%) of plugged wild-type female mice after mating with *Rnaseh1^{F/F}* and *Stra8-Rnaseh1^{-/-}* male mice (*n* = 3 independent experiments) (E). Average litter sizes were observed with *Rnaseh1^{F/F}* and *Stra8-Rnaseh1^{-/-}* male mice (*n* = 3 independent experiments) (F). Black dots indicate *Rnaseh1^{F/F}* mice, and red dots indicate *Stra8-Rnaseh1^{-/-}* mice. Data are presented as means ± SEM. two-tailed Student's t-test; ***$P < 0.001$. (**G**) The *Stra8-Rnaseh1^{-/-}* mouse testis is smaller than that of the *Rnaseh1^{F/F}* mouse. (**H**) Ratio of testis weight/body weight in *Rnaseh1^{F/F}* and *Stra8-Rnaseh1^{-/-}* mice (*n* = 4 independent experiments). Black dots indicate *Rnaseh1^{F/F}* mice and red dots indicate *Stra8-Rnaseh1^{-/-}* mice. Data are presented as means ± SEM. two-tailed Student's *t*-test; *$P < 0.05$. (**I**) Histological analysis of the seminiferous tubules and caudal epididymis of the *Rnaseh1^{F/F}* and *Stra8-Rnaseh1^{-/-}* mice by hematoxylin and eosin staining. Arrowheads indicate dead cells. (**J**) Sperm counts from the cauda epididymis significantly decreased in the *Stra8-Rnaseh1^{-/-}* mice compared with *Rnaseh1^{F/F}* mice. (n = 5 independent experiments). Black dots indicate *Rnaseh1^{F/F}* mice, and red dots indicate *Stra8-Rnaseh1^{-/-}* mice. Data are presented as means ± SEM. two-tailed Student's *t*-test; ***$P < 0.001$.
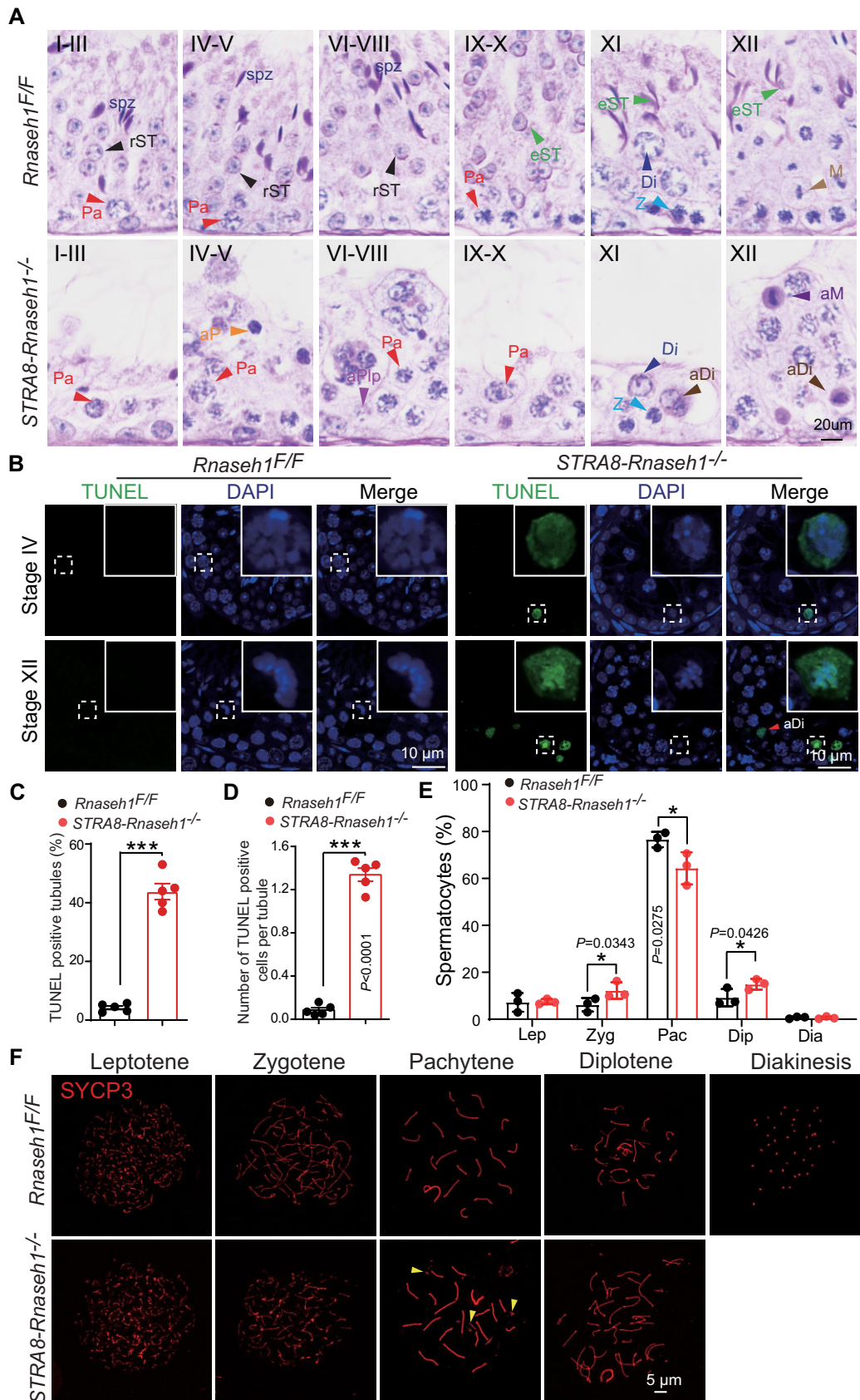
Figure 2. RNase H1 is required for meiotic prophase completion during spermatogenesis. (**A**) Germ cell-specific knockout of *Rnaseh1* causes pachytene and meiotic division arrest. Representative PAS-hematoxylin staining in *Rnaseh1^F/F* and *Stra8-Rnaseh1^−/−* seminiferous tubules. Paraffin sections from

meiotic prophase I, and *Stra8-Rnaseh1$^{-/-}$* spermatocytes display multiple defects.

To determine the exact meiotic prophase stages affected by *Rnaseh1* knockout in germ cells, we identified various stages of meiotic prophase I by staining for SYCP3, a component of the synaptonemal complex (45), and by quantifying the percentage of each prophase stage in *Rnaseh1$^{F/F}$* and *Stra8-Rnaseh1$^{-/-}$* mice. We found that the proportion of zygotene spermatocytes significantly increased, and the proportion of pachytene spermatocytes decreased in *Stra8-Rnaseh1$^{-/-}$* testes compared with that of the *Rnaseh1$^{F/F}$* testes (Figure 2E), indicating a delay of zygotene-pachytene transition in *Stra8-Rnaseh1$^{-/-}$* spermatocytes. Diplotene spermatocytes could still be observed in *Stra8-Rnaseh1$^{-/-}$* mice and showed a slight increase compared with the control groups (Figure 2E), suggesting some surviving pachytene spermatocytes might show other defects in the diplotene stage. Next, we carefully examined the morphology of the synaptonemal complex in *Rnaseh1$^{F/F}$* and *Stra8-Rnaseh1$^{-/-}$* spermatocytes. Fragmented synaptonemal complex signals have been observed in *Stra8-Rnaseh1$^{-/-}$* pachytene spermatocytes (Figure 2F), which might further cause pachytene spermatocyte death (Figures 2A–D). We observed that some spermatocytes in *Stra8-Rnaseh1$^{-/-}$* mice could further enter into diplotene stages. However, the synaptonemal complex appeared totally disassembled at almost all autosomes in *Stra8-Rnaseh1$^{-/-}$* diplotene spermatocytes (Figure 2F). In addition, some *Stra8-Rnaseh1$^{-/-}$* diplotene spermatocytes with chromosomal desynapsis were TUNEL-positive (Supplementary Figure S4D), indicating that dead diplotene and metaphase spermatocytes might be associated with premature chromosomal desynapsis. Therefore, the germ cell-specific knockout of *Rnaseh1* causes multiple defects in the meiotic prophase I, and RNase H1 is required for meiotic prophase completion during spermatogenesis.

Meiotic recombination is impaired in *stra8-rnaseh1$^{-/-}$* spermatocytes

Given that impaired chromosome recombination and synapsis often perturb meiotic prophase (46), we analyzed the efficiency of DSB formation by staining for γH2AX, which is mainly triggered by SPO11-induced meiotic DSBs (47). In both *Rnaseh1$^{F/F}$* and *Stra8-Rnaseh1$^{-/-}$* spermatocytes, γH2AX was detected at leptotene and zygotene stages (Figure 3A), suggesting that meiotic DSBs are pro-

duced independently of the RNase H1. At the pachytene stage, γH2AX persisted only on sex chromosomes in *Rnaseh1$^{F/F}$* spermatocytes, whereas γH2AX signal was still detected on the autosomes in *Stra8-Rnaseh1$^{-/-}$* spermatocytes (Figure 3A), indicating that the DSB repair is impaired in *Stra8-Rnaseh1$^{-/-}$* spermatocytes. Impaired meiotic programmed DSB repair could perturb crossover formation (48). Using immunostaining, we further observed the distribution of MLH1 foci, a marker of sites that are destined to become crossovers (49), in pachytene spermatocytes. The number of MLH1 foci was significantly reduced in *Stra8-Rnaseh1$^{-/-}$* spermatocytes compared with that of the control group (Figures 3B, C). Altogether, RNase H1 is required for meiotic recombination, and the knockout of *Rnaseh1* causes incomplete DNA repair and impaired crossover formation, finally resulting in meiotic prophase I arrest.

RNase H1 promotes the recruitment of recombinase to DSB sites

Upon meiotic DSB formation, the MRN (MRE11–RAD50–NBS1) complex is recruited to meiotic DSB sites and activates ATM (ATM phosphorylation), which is required for the DNA damage response (DDR) and further DSB resection (50–52). To clarify whether *Rnaseh1* knockout in germ cells affects the meiotic DDR and DSB resection, we monitored MRE11, NBS1 and phosphorylated ATM (p-ATM) in *Stra8-Rnaseh1$^{-/-}$* spermatocytes by examining immunofluorescence. MRE11, NBS1, and p-ATM foci were detected in both *Rnaseh1$^{F/F}$* and *Stra8-Rnaseh1$^{-/-}$* leptotene/zygotene spermatocytes (Supplementary Figure S5), indicating *Rnaseh1* knockout has little influence on the recruitment of the MRN complex and meiotic DDR.

Multiple ssDNA binding proteins (SSBs) bind to the resected ssDNA to protect it from degradation (53), and ssDNA binding protein foci could reflect the condition of DSB resection. We examined RPA, one of the SSBs, in *Rnaseh1$^{F/F}$* and *Stra8-Rnaseh1$^{-/-}$* spermatocytes. Structured illumination microscopy (SIM) observation showed that RPA foci appeared along chromosome axes in both *Rnaseh1$^{F/F}$* and *Stra8-Rnaseh1$^{-/-}$* spermatocytes (Supplementary Figure S6A). Further quantification of the RPA foci in *Stra8-Rnaseh1$^{-/-}$* spermatocytes also showed a similar level at leptotene and zygotene stages compared with those of control groups (Figures 4A, B), suggest-

---

Rnaseh1$^{F/F}$ and *Stra8-Rnaseh1$^{-/-}$* testes are stained with PAS-hematoxylin. Z: zygotene spermatocyte, Pa: pachytene spermatocyte, Di: diplotene spermatocyte, M: meiotic spermatocyte, rST: round spermatid, eST: elongating spermatid, spz: spermatozoon; aPlp: abnormal preleptotene spermatocyte; aP: abnormal pachytene spermatocyte, aDi: abnormal diplotene spermatocyte; aM: abnormal meiotic divisions. (**B**) Representative TUNEL results in *Rnaseh1$^{F/F}$* and *Stra8-Rnaseh1$^{-/-}$* stage IV and XII seminiferous tubules. Paraffin sections from *Rnaseh1$^{F/F}$* and *Stra8-Rnaseh1$^{-/-}$* testes were stained with TUNEL (**green**) and DAPI (**blue**). aDi: abnormal diplotene spermatocyte. Arrowheads indicate dead diplotene spermatocytes. (**C**) Quantification of TUNEL positive seminiferous tubules in *Rnaseh1$^{F/F}$* and *Stra8-Rnaseh1$^{-/-}$* mice (*n* = 5 independent experiments). Black dots indicate *Rnaseh1$^{F/F}$* mice, and red dots indicate *Stra8-Rnaseh1$^{-/-}$* mice. Data are presented as means ± SEM. two-tailed Student's t-test; *P < 0.05. (**D**) Quantification of TUNEL positive cell number per seminiferous tubules in *Rnaseh1$^{F/F}$* and *Stra8-Rnaseh1$^{-/-}$* mice (*n* = 5 independent experiments). Black dots indicate *Rnaseh1$^{F/F}$* mice, and red dots indicate *Stra8-Rnaseh1$^{-/-}$* mice. Data are presented as means ± SEM. two-tailed Student's t-test; ***P < 0.001. (**E**) Frequencies of meiotic stages in *Rnaseh1$^{F/F}$* and *Stra8-Rnaseh1$^{-/-}$* testis sections (n = 3 independent experiments). Lep: leptotene spermatocyte; Zyg: zygotene spermatocyte; Pac: pachytene spermatocyte; Dip: diplotene spermatocyte; Dia: Diakinesis spermatocyte. Black dots indicate *Rnaseh1$^{F/F}$* mice, and red dots indicate *Stra8-Rnaseh1$^{-/-}$* mice. Data are presented as means ± SD. two-tailed Student's *t*-test; *P < 0.05. (**F**) Immunofluorescence analysis of SYCP3 (red) is performed in *Rnaseh1$^{F/F}$* and *Stra8-Rnaseh1$^{-/-}$* spermatocyte chromosomal spreads. Arrowheads indicate fragmented synaptonemal complex signals.
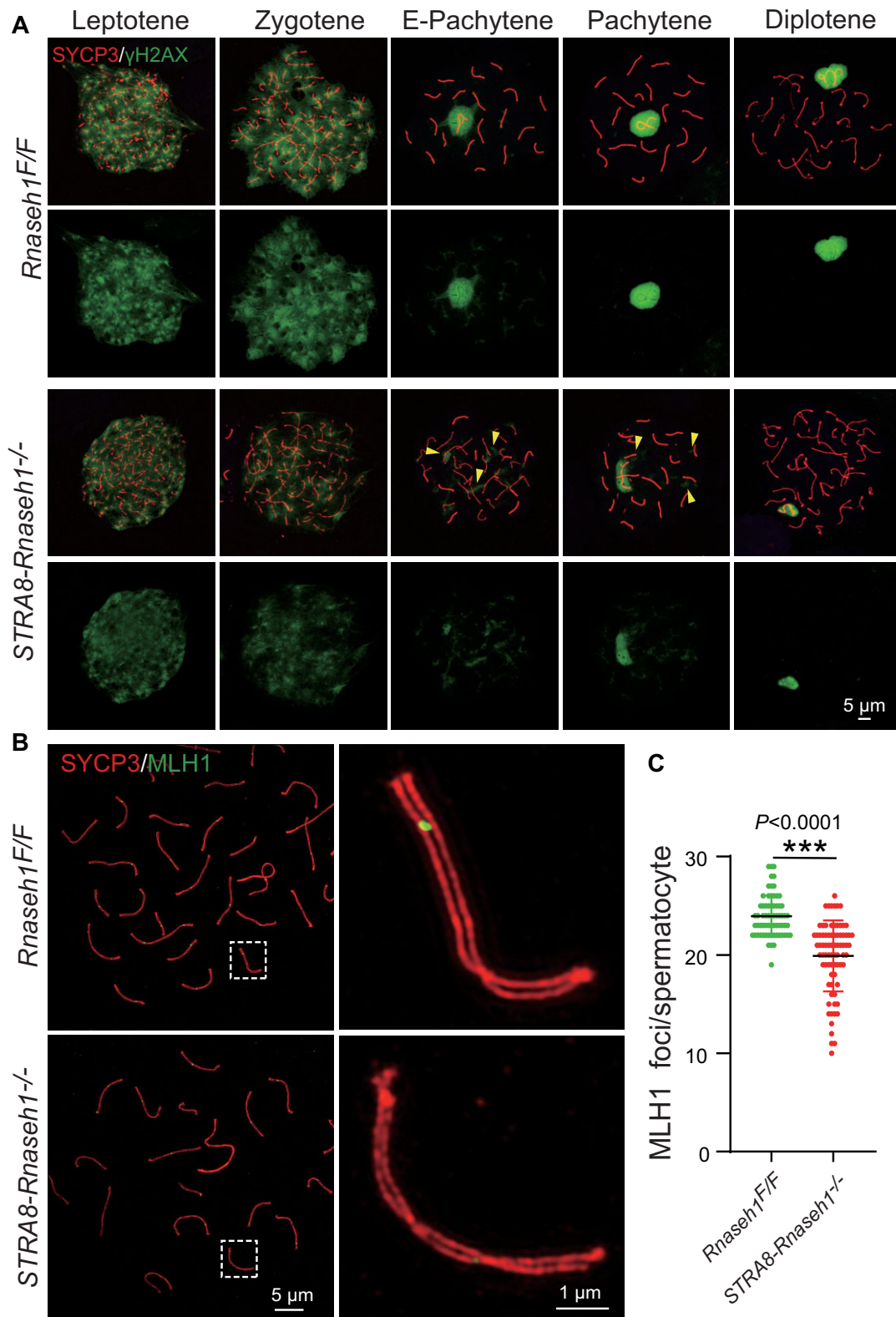
Figure 3. Germ cell-specific knockout of *Rnaseh1* impairs meiotic recombination. (**A**) Immunofluorescence analysis of SYCP3 (red) and γH2AX (green) are performed in *Rnaseh1$^{F/F}$* and *Stra8-Rnaseh1$^{-/-}$* spermatocyte chromosomal spreads. Arrowheads indicate fragmented synaptonemal complex signals. Arrowheads indicate insufficient DSB repair in autosomes. (**B**) Crossover formation is impaired in *Stra8-Rnaseh1$^{-/-}$* spermatocytes. Super-Resolution microscopy images of SYCP3 (red) and MLH1 (green) in *Rnaseh1$^{F/F}$* and *Stra8-Rnaseh1$^{-/-}$* spermatocyte chromosomal spreads. (**C**) Quantification of the MLH1 foci numbers per cell in *Rnaseh1$^{F/F}$* ($n = 67$ independent experiments) and *Stra8-Rnaseh1$^{-/-}$* spermatocytes ($n = 78$ independent experiments). Green dots indicated *Rnaseh1$^{F/F}$* spermatocytes, and red dots indicated *Stra8-Rnaseh1$^{-/-}$* spermatocytes. Data are presented as means ± SD. two-tailed Student's *t*-test; ***$P < 0.001$.
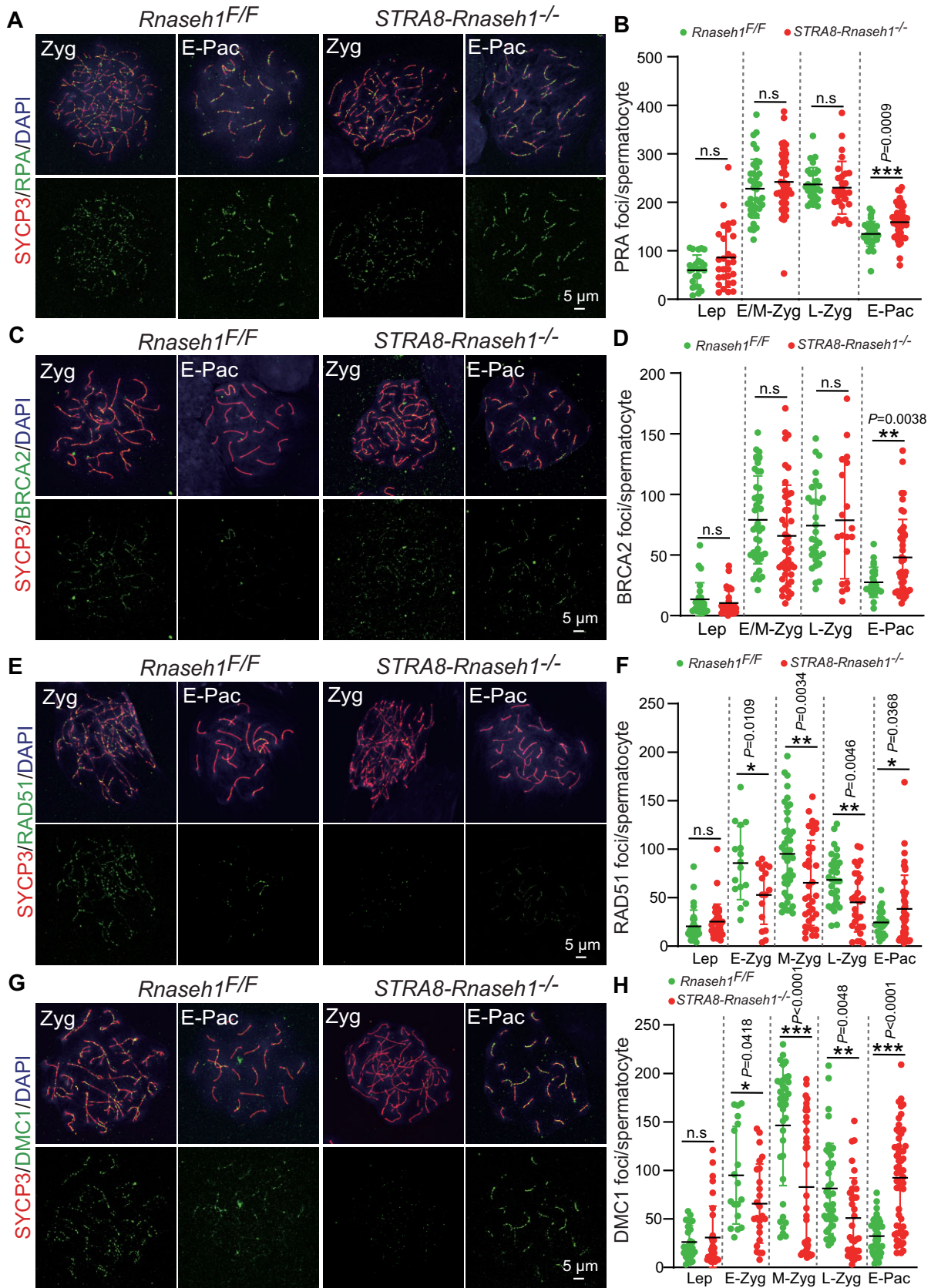
Figure 4. RNase H1 participates in the recruitment of recombinases. (**A**) Immunofluorescence analysis of SYCP3 (red) and RPA (green) are performed in *Rnaseh1^{F/F}* and *Stra8-Rnaseh1^{−/−}* spermatocyte chromosomal spreads. Nuclei are stained with DAPI (blue). Zyg: zygotene spermatocyte; E-Pac: early-

ing the knockout of *Rnaseh1* was dispensable for DSB resection and RPA binding to resected ssDNA. SPATA22 and MEIOB, two meiosis-specific SSB (24,54), showed a similar phenomenon in *Stra8-Rnaseh1*$^{-/-}$ leptotene and zygotene spermatocytes (Supplementary Figures S7B–F). These results suggest that the germ cell-specific knockout of *Rnaseh1* has little effect on DSB resection and the recruitment of SSBs on DSB ends. However, the number of RPA, SPATA22, and MEIOB foci appeared to increase slightly in *Stra8-Rnaseh1*$^{-/-}$ early-pachytene spermatocytes (Figure 4B and Supplementary Figures S6D, F), indicating the insufficient DSB repair in *Stra8-Rnaseh1*$^{-/-}$ spermatocytes.

SPATA22-MEIOB could recruit BRCA2 via MEILB2-BRME1, which further promotes the loading of recombinases, RAD51 and DMC1, onto the ssDNA (23,55–57) for strand invasion (58,59). Next, we examined the recruitment of BRCA2 in *Stra8-Rnaseh1*$^{-/-}$ spermatocytes and found the number of BRCA2 foci in *Stra8-Rnaseh1*$^{-/-}$ leptotene and zygotene spermatocytes were similar to that of the control groups (Figures 4C, D), revealing that the knockout of *Rnaseh1* does not affect the recruitment of BRCA2. Consistent with RPA, SPATA22, and MEIOB, the elevated BRCA2 foci were also observed in *Stra8-Rnaseh1*$^{-/-}$ early-pachytene spermatocytes (Figures 4D).

Next, we examined the recruitment of RAD51 and DMC1 recombinases in *Stra8-Rnaseh1*$^{-/-}$ spermatocytes and detected significantly decreased foci numbers of both RAD51 and DMC1 recombinases in *Stra8-Rnaseh1*$^{-/-}$ zygotene spermatocytes (Figures 4E–H and Supplementary Figure S7A, B). To exclude the indirect effects of *RNaseh1* knockout that caused reduced RAD51 and DMC1 foci, we first examined the protein level of RAD51 and DMC1 in *Rnaseh1*$^{F/F}$ and *Stra8-Rnaseh1*$^{-/-}$ testes and found that *Rnaseh1* knockout has little effect on the expression of RAD51 and DMC1 (Supplementary Figure S7C–E). We further quantified RAD51 and DMC1 foci during each zygotene stage to more fully understand the formation and maintenance of recombinase foci (54,60). In *Rnaseh1*$^{F/F}$ spermatocytes, RAD51 and DMC1 foci started increasing at the early-zygotene stage, showed maximum levels during the middle-zygotene stage, and decreased over the course of the early-pachytene stage (Figure 4F, H). In *Stra8-Rnaseh1*$^{-/-}$ spermatocytes, RAD51 and DMC1 foci significantly decreased as early as in the early-zygotene stage compared with those of control groups (Figures 4F, H), indicating that RNase H1 might be participating in RAD51 and DMC1 foci formation. Given that recombinase foci could be observed in *Stra8-Rnaseh1*$^{-/-}$ early-pachytene spermatocytes (Figures 4F, H), the knockout of *Rnaseh1* might alter the dynamics of recombinase loading during meiosis. These findings suggest that RNase H1 might promote the recruitment of recombinase during meiotic recombination.

The foci number of recombinase appeared to increase in *Stra8-Rnaseh1*$^{-/-}$ early-pachytene spermatocytes (Figures 4F, H), suggesting that the persistent BRCA2 may overcome the effects of *Rnaseh1* knockout on recombinase recruitment. However, SIM images of RAD51 and DMC1 in *Stra8-Rnaseh1*$^{-/-}$ early-pachytene spermatocytes showed that some recombinases could be observed on non-homologous chromosome axes (Supplementary Figure S7A, B). In addition, HEI10, a pro-crossover protein (61,62), could be observed in non-homologous pairing within *Stra8-Rnaseh1*$^{-/-}$ spermatocytes (Supplementary Figure S7F). As at least one partner is a non-homolog, the non-homologous repair is taking place in

---

pachytene spermatocyte. (**B**) Quantification of the RPA foci per cell in *Rnaseh1*$^{F/F}$ and *Stra8-Rnaseh1*$^{-/-}$ spermatocytes. Lep: leptotene spermatocyte ($n = 24$, 29 independent experiments for *Rnaseh1*$^{F/F}$ and *Stra8-Rnaseh1*$^{-/-}$, respectively); E/M-Zyg: early or middle zygotene spermatocyte ($n = 38$, 47 independent experiments for *Rnaseh1*$^{F/F}$ and *Stra8-Rnaseh1*$^{-/-}$, respectively); L-Zyg: late zygotene spermatocyte ($n = 29$, 28 independent experiments for *Rnaseh1*$^{F/F}$ and *Stra8-Rnaseh1*$^{-/-}$, respectively); E-Pac: early-pachytene spermatocyte ($n = 33$, 46 independent experiments for *Rnaseh1*$^{F/F}$ and *Stra8-Rnaseh1*$^{-/-}$, respectively). Green dots indicate *Rnaseh1*$^{F/F}$ spermatocytes, and red dots indicate *Stra8-Rnaseh1*$^{-/-}$ spermatocytes. Data are presented as means ± SD. two-tailed Student's *t*-test; ns: no significance; ***$P < 0.001$. (**C**) Immunofluorescence analysis of SYCP3 (red) and BRCA2 (green) are performed in *Rnaseh1*$^{F/F}$ and *Stra8-Rnaseh1*$^{-/-}$ spermatocyte chromosomal spreads. Nuclei are stained with DAPI (blue). Zyg: zygotene spermatocyte; E-Pac: early-pachytene spermatocyte. (**D**) Quantification of the BRCA2 foci per cell in *Rnaseh1*$^{F/F}$ and *Stra8-Rnaseh1*$^{-/-}$ spermatocytes. Lep: leptotene spermatocyte ($n = 25$, 28 independent experiments for *Rnaseh1*$^{F/F}$ and *Stra8-Rnaseh1*$^{-/-}$, respectively); E/M-Zyg: early or middle zygotene spermatocyte ($n = 46$, 44 independent experiments for *Rnaseh1*$^{F/F}$ and *Stra8-Rnaseh1*$^{-/-}$, respectively); L-Zyg: late zygotene spermatocyte ($n = 31$, 19 independent experiments for *Rnaseh1*$^{F/F}$ and *Stra8-Rnaseh1*$^{-/-}$, respectively); E-Pac: early-pachytene spermatocyte ($n = 23$, 46 independent experiments for *Rnaseh1*$^{F/F}$ and *Stra8-Rnaseh1*$^{-/-}$, respectively). Green dots indicate *Rnaseh1*$^{F/F}$ spermatocytes and red dots indicate *Stra8-Rnaseh1*$^{-/-}$ spermatocytes. Data are presented as means ± SD. two-tailed Student's *t* test; ns: no significance; **$P < 0.01$. (**E**) Immunofluorescence analysis of SYCP3 (red) and RAD51 (green) are performed in *Rnaseh1*$^{F/F}$ and *Stra8-Rnaseh1*$^{-/-}$ spermatocyte chromosomal spreads. Nuclei are stained with DAPI (**blue**). Zyg: zygotene spermatocyte; E-Pac: early-pachytene spermatocyte. (**F**) Quantification of the RAD51 foci per cell in *Rnaseh1*$^{F/F}$ and *Stra8-Rnaseh1*$^{-/-}$ spermatocytes. Lep: leptotene spermatocyte ($n = 31$, 34 independent experiments for *Rnaseh1*$^{F/F}$ and *Stra8-Rnaseh1*$^{-/-}$, respectively); E-Zyg: early zygotene spermatocyte ($n = 16$ independent experiments for *Rnaseh1*$^{F/F}$ and *Stra8-Rnaseh1*$^{-/-}$); M-Zyg: middle zygotene spermatocyte ($n = 43$, 36 independent experiments for *Rnaseh1*$^{F/F}$ and *Stra8-Rnaseh1*$^{-/-}$, respectively); L-Zyg: late zygotene spermatocyte ($n = 31$, 29 independent experiments for *Rnaseh1*$^{F/F}$ and *Stra8-Rnaseh1*$^{-/-}$, respectively); E-Pac: early-pachytene spermatocyte ($n = 30$, 44 independent experiments for *Rnaseh1*$^{F/F}$ and *Stra8-Rnaseh1*$^{-/-}$, respectively). Green dots indicate *Rnaseh1*$^{F/F}$ spermatocytes, and red dots indicate *Stra8-Rnaseh1*$^{-/-}$ spermatocytes. Data are presented as means ± SD. two-tailed Student's *t*-test; ns: no significance; *$P < 0.05$; **$P < 0.01$; ***$P < 0.001$. (**G**) Immunofluorescence analysis of SYCP3 (red) and DMC1 (green) are performed in *Rnaseh1*$^{F/F}$ and *Stra8-Rnaseh1*$^{-/-}$ spermatocyte chromosomal spreads. Nuclei are stained with DAPI (blue). Zyg: zygotene spermatocyte; E-Pac: early-pachytene spermatocyte. (**H**) Quantification of the DMC1 foci per cell in *Rnaseh1*$^{F/F}$ and *Stra8-Rnaseh1*$^{-/-}$ spermatocytes. Lep: leptotene spermatocyte ($n = 26$, 32 independent experiments for *Rnaseh1*$^{F/F}$ and *Stra8-Rnaseh1*$^{-/-}$, respectively); E-Zyg: early zygotene spermatocyte ($n = 18$, 25 independent experiments for *Rnaseh1*$^{F/F}$ and *Stra8-Rnaseh1*$^{-/-}$, respectively); M-Zyg: middle zygotene spermatocyte ($n = 37$, 33 independent experiments for *Rnaseh1*$^{F/F}$ and *Stra8-Rnaseh1*$^{-/-}$, respectively); L-Zyg: late zygotene spermatocyte ($n = 39$, 33 independent experiments for *Rnaseh1*$^{F/F}$ and *Stra8-Rnaseh1*$^{-/-}$, respectively); E-Pac: early-pachytene spermatocyte ($n = 41$, 55 independent experiments for *Rnaseh1*$^{F/F}$ and *Stra8-Rnaseh1*$^{-/-}$, respectively). Green dots indicate *Rnaseh1*$^{F/F}$ spermatocytes, and red dots indicate *Stra8-Rnaseh1*$^{-/-}$ spermatocytes. Data are presented as means ± SD. two-tailed Student's *t*-test; ns: no significance; **$P < 0.01$; ***$P < 0.001$.

Stra8-Rnaseh1$^{-/-}$ spermatocytes, which may further lead to pachytene spermatocyte death.

DNA–RNA hybrids accumulate in *stra8-rnaseh1*$^{-/-}$ spermatocytes

To explore the function of RNase H1 on recombinase loading during meiotic recombination, we used immunoblotting to first examine its expression in mouse testis. We found RNase H1 was detectable in testes at PD2, and levels kept increasing from PD14 onward and reached maximum levels at PD21 (Figure 5A), indicating RNase H1 was predominantly expressed in spermatocytes. Further immunoblotting and immunostaining showed similar results (Figures 5B, C, Supplementary Figure S2B). Next, we characterized the precise localization of RNase H1 in spermatocyte chromosomal spreads using immunofluorescence. At leptotene and zygotene stages, RNase H1 showed punctate signals, and some RNase H1 foci localized along chromosome axes (Figure 5D). RNase H1 signals reached maximum levels at the pachytene stage, and its signals were absent in *Stra8-Rnaseh1*$^{-/-}$ spermatocytes (Figure 5D). Thus, RNase H1 dynamically localizes on meiotic chromosomes in meiosis prophase I.

As RNase H1 is essential for meiotic recombination, we further tested whether the RNase H1 signals along chromosome axes in the zygotene stage are dependent on meiotic DSB formation. Pursuing this, we detected the localization of RNase H1 in *Spo11*$^{-/-}$ spermatocytes, which abolished meiotic DSBs generation (47). We found RNase H1 foci along chromosome axes disappeared after SPO11 depletion (Figure 5E), and RNase H1 protein levels also dramatically decreased in *Spo11*$^{-/-}$ PD12 testis (Figure 5F). Therefore, RNase H1 foci along chromosome axes are highly associated with meiotic DSB formation. We also noticed that RNase H1 foci along chromosome axes could still be observed in *Dmc1*$^{-/-}$ spermatocytes (Figure 5G), and the protein level of RNase H1 in *Dmc1*$^{-/-}$ testis were similar with that of control groups (Figure 5G). In addition, the signals of HOP2, which binds with DMC1 and is required for accurate homology searching in the DMC1-dependent pathway (63,64), were dramatically reduced in *Stra8-Rnaseh1*$^{-/-}$ spermatocytes (Supplementary Figure S8A), which was similar to *Dmc1*$^{-/-}$ spermatocytes (Supplementary Figure S8A). As the *Rnaseh1* knockout impairs DMC1 loading (Figures 4G, H), RNase H1 might function upstream of DMC1 during meiotic recombination.

Given that RNase H1 is a key modulator for DNA–RNA hybrid homeostasis by degrading the RNA within DNA–RNA hybrids (9), we examined the hybrid level in spermatocyte chromosomal spreads using the immunofluorescence of S9.6 antibody, which is effective in the identification of DNA–RNA hybridization (65). DNA–RNA hybrids were widely observed in the nuclei of leptotene spermatocytes, and some DNA–RNA hybrid punctate signals appeared along chromosome axes (Figures 5I, J). RNase A treatment totally abolished DNA–RNA hybrid signals in spermatocyte chromosomal spreads (Figure 5I). We also examined the localization of DNA–RNA hybrids in *Spo11*$^{-/-}$ spermatocytes and found the DNA–RNA hybrid signals along chromosome axes disappeared (Figure 5K). In addition, we noticed that DNA–RNA hybrids in wild-type spermatocytes were adjacent to RPA, RAD51, and DMC1 (Supplementary Figures S8B–G). Our findings suggest DNA–RNA hybrids can form near meiotic DSB sites, and hybrid generation is highly associated with meiotic DSB formation.

DNA–RNA hybrid signals exhibited a slight decrease and localized on the chromosome axes at zygotene and pachytene stages (Figures 5I, J), showing the opposite tendency of RNase H1. In *Stra8-Rnaseh1*$^{-/-}$ spermatocytes, DNA–RNA hybrid signals significantly increased (Figures 5I, J), especially with chromosome axis signals at zygotene and pachytene stages (Figure 5I). In addition, DNA–RNA hybrid signals that were adjacent to RPA were dramatically elevated in *Stra8-Rnaseh1*$^{-/-}$ spermatocytes (Supplementary Figure S8B). Thus, the germ cell-specific knockout of *Rnaseh1* causes the accumulation of DNA–RNA hybrids in meiosis prophase I, and RNase H1 modulates the DNA–RNA hybrid homeostasis during the meiotic recombination.

RNase H1 promotes recombinase recruitment by digesting DNA–RNA hybrids

DNA–RNA hybrids have been shown to form in DNA damage sites (66). Given that germ cell-specific knockout of *Rnaseh1* led to DNA–RNA hybrid accumulation (Figure 5) and altered the dynamics of RAD51 and DMC1 loading on DSB sites (Figures 4E-H), we speculated that RNase H1 might promote recombinase loading by processing DNA–RNA hybrids. To test this hypothesis, we examined the effect of RNase H1 on recombinase loading onto DNA–RNA hybrids at the single-molecule level. To this end, we employed dual-optical traps combined with confocal microscopy to record the length of a DNA–RNA hybrid molecule and the fluorescence signals of recombinases in real time (Figure 6A) (67). In this experiment, a single DNA–RNA hybrid molecule (7.4 kb) was suspended between one fixed trap and one steered trap via two streptavidin-coated microspheres, and a high-frequency feedback system on the steered trap was employed to ensure the force on the hybrid remained constant. Once RNase H1 degrades the RNA within the DNA–RNA hybrid, the hybrid length would increase under tension (Figure 6A), and fluorescently labeled recombinases bound to ssDNA could be monitored (68).

We started this experiment at a force of 10 pN with 5 nM of RNase H1. As expected, the hybrid length continuously increased, starting at 10 seconds(s) and leveling off at about 100 s (Figure 6B). In addition, the molecule extension rate increased from 10.9 ± 0.9 to 33.8 ± 4.9 nm/s when the RNase H1 concentration was increased from 5 to 50 nM (Figure 6B). These changes in the hybrid length reflect the DNA–RNA hybrid degradation activity of RNase H1.

Next, we examined the loading of RAD51 onto the hybrid by using the fluorescently labeled (Alexa Fluor 55) protein RAD51-AF555. The presence of 300 nM of RAD51-AF555 caused a slow increase in the hybrid length at a rate of 0.8 ± 0.2 nm/s over 120 s. Concurrently, the fluorescence signal along the DNA–RNA hybrid was minimal (Figures 6C, D). These mechanical and fluorescent findings support that RAD51 is barely loaded onto the DNA–RNA hybrid
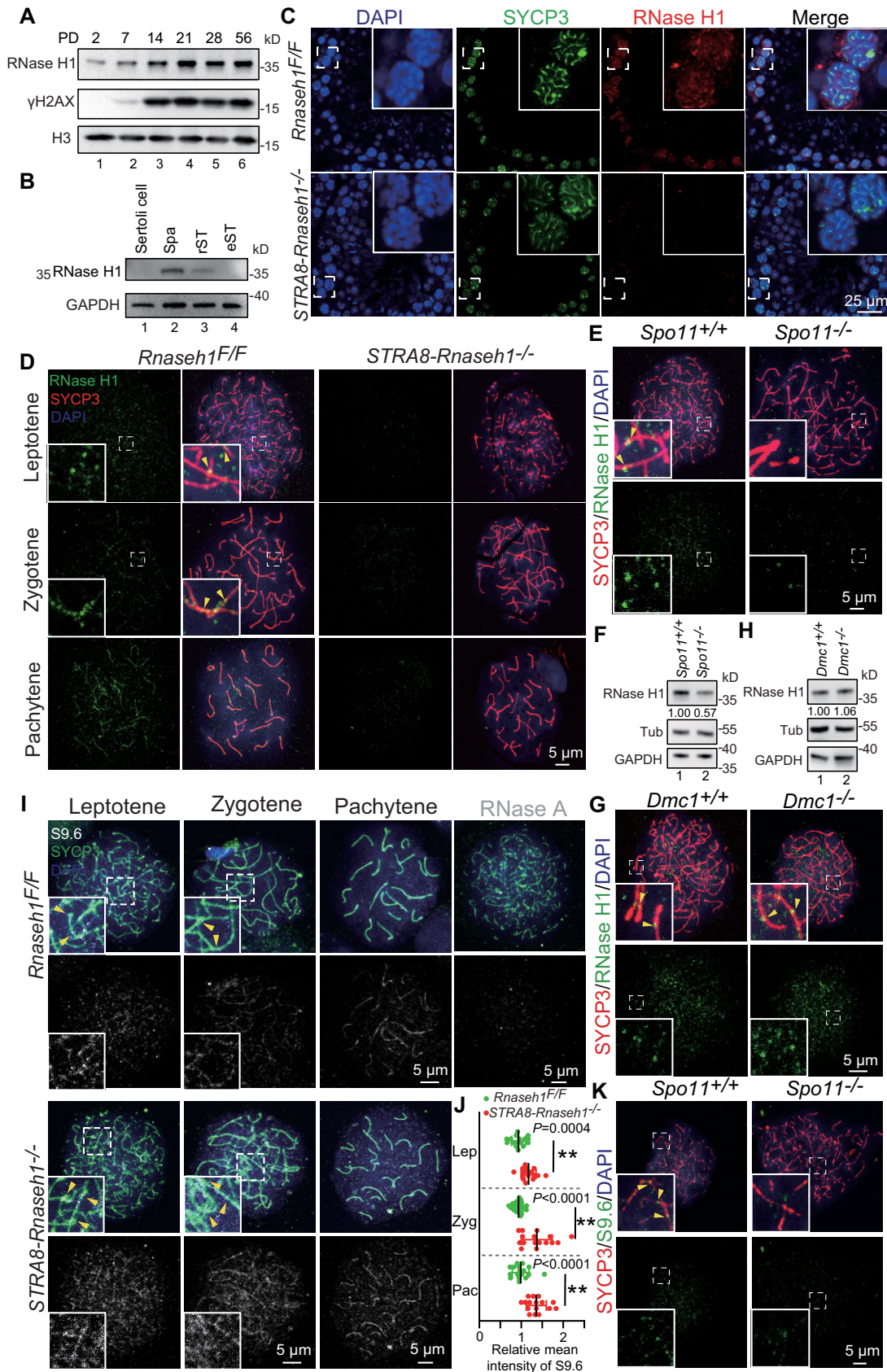
Figure 5. DNA–RNA hybrids accumulated in *Stra8-Rnaseh1*$^{-/-}$ spermatocytes. (**A**) Immunoblotting analysis of RNase H1 protein from various postnatal testis. H3 serves as the loading control. (**B**) RNase H1 is predominantly expressed in spermatocytes. Immunoblotting of RNase H1 is performed in

under these conditions. In stark contrast, the presence of 20 nM of RNase H1 caused a rapid increase in the hybrid length that plateaued after 60 seconds, occurring at a rate of 23.7 ± 0.9 nm/s, which was comparable to the rate of 20.3 ± 4.3 nm/s observed with 20 nM of RNase H1 only (Figures 6B, C). Meanwhile, the RAD51-AF555 fluorescent signal along the DNA–RNA hybrid appeared and was quickly saturated (Figures 6C, D), suggesting the molecule was entirely coated by RAD51. These observations indicate RNase H1 indeed facilitates the loading of RAD51 onto the hybrid.

Using the same experimental conditions, we investigated another recombinase, DMC1. In the presence of 300 nM of DMC1 labeled with an enhanced green fluorescent protein (DMC1-eGFP), the hybrid length showed no apparent changes, and the fluorescence signal was not detected along the hybrid. Nevertheless, the addition of 20 nM RNase H1 promotes a rapid increase in the hybrid length at a rate of 17.4 ± 2.6 nm/s and leads to a complete coating of DMC1 onto the molecule within 90 s (Figures 6E, F). Therefore, RNase H1 directly facilitates recombinase loading onto the DNA–RNA hybrid.

DISCUSSION

Meiotic recombination is critical for genetic diversity and successful sperm production, is initiated through programmed DSBs and requires many recombination factors to be recruited and facilitated for homology-directed DNA repair (69–71). Emerging evidence suggests that DNA–RNA hybrids participate in DNA repair (6,72), could directly form in DNA damage sites (66) and might facilitate DNA repair by protecting 3′ overhangs, recruiting recombination factors, enhancing D-loops formation, and inducing RNA-template-dependent repair (1,6,66,72–77). Here, we found that DNA–RNA hybrids were widely detected in the nuclei of spermatocytes, and some DNA–RNA hybrid punctate signals appeared along chromosome axes at leptotene and zygotene stages in the SPO11-dependent pathway (Figure 5D). Germ cell-specific knockout of *Rnaseh1* causes the accumulation of DNA–RNA hybrids in meiosis prophase I, which altered the dynamics of RAD51 and DMC1 recombinase loading on DSB sites (Figure 4, Supplementary Figure S7).

As for the relationship between RAD51 and DMC1 recombinase loading and accumulated DNA–RNA hybrids, we have demonstrated that DNA–RNA hybrids directly inhibit RAD51 and DMC1 loading by *in vitro* experiments (Figure 6). We further examined localizations of RAD51/DMC1 and DNA–RNA hybrids, and found that DNA–RNA hybrids were adjacent to RAD51 and DMC1, but not completely co-localized with each other (Supplementary Figure S8D-G). Even in *Stra8-Rnaseh1$^{-/-}$* spermatocytes, the accumulated DNA–RNA hybrids were still partially co-localized with RPA (Supplementary Figure S8B). Therefore, DNA–RNA hybrids may not be fully formed in the resected ssDNA because some recombinases still could be loaded onto meiotic DSB ends. Accumulated DNA–RNA hybrids in *Stra8-Rnaseh1$^{-/-}$* spermatocytes might inhibit further assembly of recombinases near the meiotic DSB regions.

Both aforementioned hypotheses raise a key question: do DNA–RNA hybrids physically block recombinase loading onto DNA–RNA hybrids? Our single-molecule data provide direct evidence to show that RAD51 and DMC1 recombinases are incapable of directly recognizing and loading onto DNA–RNA hybrids, and RNase H1-mediated DNA–RNA hybrid digestion promotes RAD51 and DMC1 nucleoprotein filament formation (Figures 6C–F). Thus, DNA–RNA hybrids prevent recombinases from loading and this prevention might be relieved by RNase H1 degrading RNA in DNA–RNA hybrids, further promoting meiotic recombination (Figure 7).

RAD51 and DMC1 are key recombinases during meiotic recombination, which bind to the 3′ssDNA overhangs around DSB sites to form nucleoprotein filaments. RAD51 and DMC1 nucleoprotein filaments search for the matching sequence on the homologous chromosome and carry out strand invasion (78,79). Distinctive roles of RAD51 and DMC1 recombinases in meiotic recombination have been identified (58,80,81). We found that the knockout of *Rnaseh1* has different effects on RAD51 and DMC1 during the early-pachytene stage. More DMC1 foci were observed than RAD51 foci (Figures 4E–H). Given that DMC1 binds near DNA break sites (81) and germ cell-specific knockout of *Rnaseh1* has little effect on the recruitment of ssDNA binding proteins and BRCA2 after DSB resection (Figures 4A–D and Supplementary Figure S6), DNA–RNA hybrids may occur farther away from DNA break sites and nearer to junctions with dsDNA. Indeed, DNA–RNA hybrids were adjacent to RPA, RAD51 and DMC1 (Supplementary Figures S8B-G). In addition, DMC1 shows a higher mismatch tolerance than RAD51 (80), and the recruitment of DMC1 in *Stra8-Rnaseh1$^{-/-}$* early-pachytene

---

Sertoli cells, spermatocytes (spa), round spermatids (rST), and elongated spermatids (eST). GAPDH serves as the loading control. (**C**) Immunofluorescence analysis of SYCP3 (green) and RNase H1 (red) are performed in *Rnaseh1$^{F/F}$* and *Stra8-Rnaseh1$^{-/-}$* testis. Nuclei are stained with DAPI (blue). (**D**) Immunofluorescence analysis of SYCP3 (red) and RNase H1 (green) are performed in *Rnaseh1$^{F/F}$* and *Stra8-Rnaseh1$^{-/-}$* spermatocyte chromosomal spreads. Nuclei are stained with DAPI (blue). Arrowheads indicate RNase H1 signals along chromosome axes. (**E**) Immunofluorescence analysis of SYCP3 (red) and RNase H1 (green) are performed in *Spo11$^{+/+}$* and *Spo11$^{-/-}$* spermatocyte chromosomal spreads. Nuclei are stained with DAPI (blue). Arrowheads indicate RNase H1 signals along chromosome axes. (**F**) Immunoblotting of RNase H1 is performed in *Spo11$^{+/+}$* and *Spo11$^{-/-}$* testes. Tubulin and GAPDH serves as the loading control. (**G**) Immunofluorescence analysis of SYCP3 (red) and RNase H1 (green) are performed in *Dmc1$^{+/+}$* and *Dmc1$^{-/-}$* spermatocyte chromosomal spreads. Nuclei are stained with DAPI (blue). Arrowheads indicate RNase H1 signals along chromosome axes. (**H**) Immunoblotting of RNase H1 is performed in *Dmc1$^{+/+}$* and *Dmc1$^{-/-}$* testes. Tubulin and GAPDH serves as the loading control. (**I**) Immunofluorescence analysis of SYCP3 (green) and S9.6 (white) are performed in *Rnaseh1$^{F/F}$* and *Stra8-Rnaseh1$^{-/-}$* spermatocyte chromosomal spreads. Nuclei are stained with DAPI (blue). Arrowheads indicate S9.6 signals along chromosome axes. (**J**) Quantification of the relative mean intensity of S9.6 in *Rnaseh1$^{F/F}$* and *Stra8-Rnaseh1$^{-/-}$* spermatocytes. Data are presented as means ± SD. two-tailed Student's *t*-test; **$P < 0.01$. (**K**) Immunofluorescence analysis of SYCP3 (red) and S9.6 (green) are performed in *Spo11$^{+/+}$* and *Spo11$^{-/-}$* spermatocyte chromosomal spreads. Nuclei are stained with DAPI (blue). Arrowheads indicate S9.6 signals along chromosome axes.
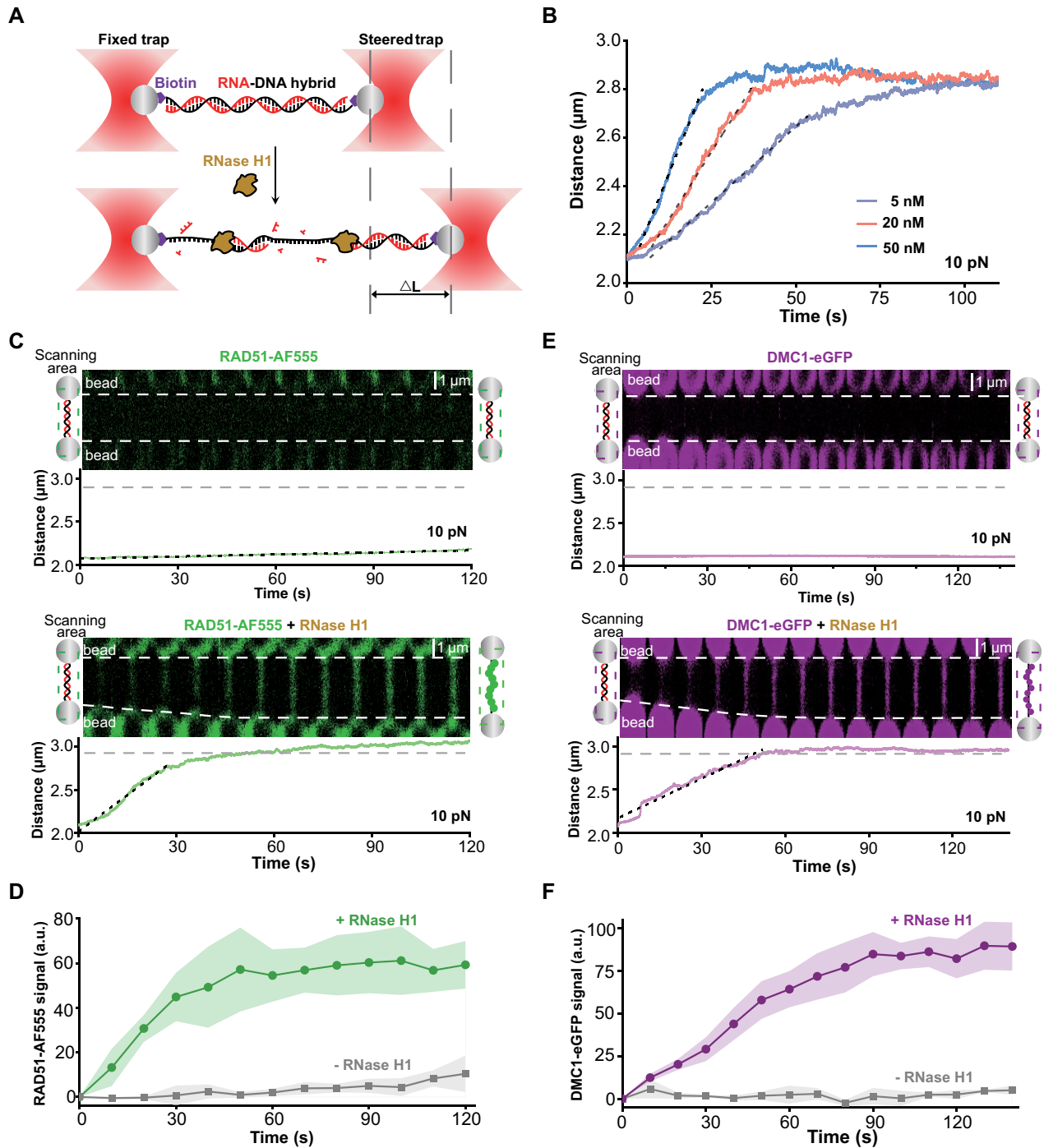
Figure 6. RNase H1 promotes recombinase recruitment by degrading DNA–RNA hybrids. (**A**) A schematic of the experimental configuration. A biotinylated 7.4-kb DNA–RNA hybrid is suspended between two streptavidin-coated beads, which are manipulated by two optical traps. DNA length is expected to increase when the suspended DNA–RNA hybrid is degraded to ssDNA by RNase H1. (**B**) The DNA–RNA hybrid template length as a function of time in the presence of 5, 20 and 50 nM RNase H1. A linear fit is shown as a black dotted line. (**C**) Representative kymographs showing RAD51-AF555 signal on the DNA–RNA hybrid in the absence (top) and presence (bottom) of 20 nM RNase H1. The corresponding length of the examined molecule under 10 pN is shown below the kymograph. A linear fit is shown as a black dotted line. (**D**) Real-time fluorescence intensities of RAD51-AF555 along the DNA–RNA hybrid in the absence (gray) and presence (green) of 20 nM RNase H1. The shaded area represents SEM ($n \geq 5$). (**E**) Representative kymographs showing DMC1-eGFP signal on the DNA–RNA hybrid in the absence (top) and presence (bottom) of 20 nM RNase H1. The corresponding length of the examined molecule under 10 pN is shown below the kymograph. A linear fit is shown as a black dotted line. (**F**) Real-time fluorescence intensities of DMC1-eGFP along the DNA–RNA hybrid in the absence (gray) and presence (purplish red) of 20 nM RNase H1. The shaded area represents SEM ($n \geq 5$).
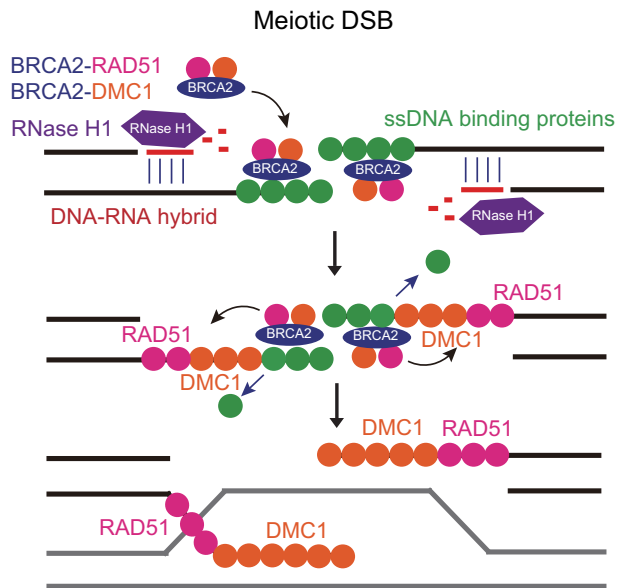
Figure 7. A proposed model for the functional role of RNase H1 during meiotic recombination. DNA–RNA hybrids could be formed near meiotic DSB sites and prevent recombinases from loading. RNase H1 could directly remove the DNA–RNA hybrids and facilitate RAD51 and DMC1 nucleoprotein filaments formation, which search for the matching sequence on the homologous chromosome and carry out strand invasion.

spermatocytes may cause non-homologous repair (Supplementary Figures S7A, B and F), impairing proper crossover formation and leading to meiotic arrest.

Given that, during yeast meiosis, accumulated DNA–RNA hybrids have been shown to influence the accumulation of Rad51p and Dmc1p around DSB sites (82), DNA–RNA hybrids may play a similar role in mouse meiotic recombination. In yeast, DNA–RNA hybrids were poorly detected in *RNH1* (the homolog of *Rnaseh1*), and deletion strains and *rnh1Δ* cells showed little effect on yeast sporulation (82). In contrast, our studies showed elevated DNA–RNA hybrid levels in *Stra8-Rnaseh1*$^{-/-}$ spermatocytes (Figure 5I, J), and germ cell-specific knockout of *Rnaseh1* showed severe defects in mouse spermatogenesis, causing male infertility (Figure 1). Therefore, mammalian spermatocytes appear more sensitive to perturbed DNA–RNA hybrid homeostasis. Furthermore, accumulated DNA–RNA hybrids in yeast meiosis have no effect on Rad51p foci but influence their intensity and enrichment around DSB sites. DNA–RNA hybrid foci were found to colocalize with RPA foci (82). However, in *Stra8-Rnaseh1*$^{-/-}$ zygotene mouse spermatocytes, RAD51 and DMC1 foci significantly decreased (Figure 4E–H), and DNA–RNA hybrid signals were adjacent to but not colocalized with RPA foci (Supplementary Figure S8B–G). These findings indicate yeast and mice recruit recombinases in different ways.

In fission yeast DSB repair processes, deletion of RNase H1 and RNase H2 stabilizes DNA–RNA hybrids and impairs the recruitment of RPA complexes around DSB sites (73). In human somatic cells, a lack of EXOSC10 causes increased DNA–RNA hybrid levels, which further perturbs RPA recruitment to DSB sites (83). However, germ cell-specific *Rnaseh1* knockout in mice has little effect on

the recruitment of SSBs after DSB resection during meiotic recombination (Figures 4A, B, and Supplementary Figure S4). A similar phenomenon was observed during yeast meiosis in *rnh1Δ/rnh201Δ/hpr1Δ* triple mutant cells (82). Therefore, the effects and regulation mechanism(s) of DNA–RNA hybrids on SSBs recruitment should be different in mitotic DSB repair and meiotic recombination.

The DNA–RNA hybrid helicase, Senataxin, has also been reported to participate in meiotic recombination and MSCI during mouse spermatogenesis (18,19). Different from *Rnaseh1*, the knockout of *Setx* impaired disassembly of RAD51 filaments, and totally abolished crossover formation in mouse meiosis (18). In addition, Senataxin was critical for ATR and CHD4-mediated sex chromosome transcriptional silencing and chromatin remodeling during meiosis (19). Different roles of RNase H1 and Senataxin in meiosis may be due to their different expression pattern and localization in mouse spermatocytes, as Senataxin mainly localized on the XY body at the pachytene stage (18), while RNase H1 showed punctate signals and appeared along chromosome axes at leptotene and zygotene stages (Figure 5C).

Except for meiotic recombination, germ cell-specific knockout of *Rnaseh1* also shows multiple defects during spermatogenesis. Elevated DNA damage and cell death could be observed in some *Stra8-Rnaseh1*$^{-/-}$ preleptotene spermatocytes (Supplementary Figure S4), which might be due to accumulated DNA–RNA hybrids inducing replication stress (17,84). In the *C. elegans* germline, DNA–RNA hybrid accumulation leads to irreparable DSB formation, which could progress into meiosis and propagate in oocytes (17). Therefore, the DNA–RNA hybrid accumulation in *Stra8-Rnaseh1*$^{-/-}$ preleptotene spermatocytes might also lead to irreparable DSBs and further impair the meiotic process. The knockout of RNase H1 also caused premature chromosomal desynapsis at the diplotene stage (Figure 2F), indicating, except for meiotic recombination, that RNase H1 localized to chromosome axes might also participate in synaptonemal complex stabilization. Thus, DNA–RNA hybrids and their regulators may play multiple roles during spermatogenesis.

DATA AVAILABILITY

All data generated or analyzed during this study are included in this article and its supplementary data.

SUPPLEMENTARY DATA

Supplementary Data are available at NAR Online.

ACKNOWLEDGEMENTS

REFERENCES

1. Petermann,E., Lan,L. and Zou,L. (2022) Sources, resolution and physiological relevance of R-loops and RNA-DNA hybrids. *Nat. Rev. Mol. Cell Biol.*, **23**, 521–540.
2. Niehrs,C. and Luke,B. (2020) Regulatory R-loops as facilitators of gene expression and genome stability. *Nat. Rev. Mol. Cell Biol.*, **21**, 167–178.
3. Mackay,R.P., Xu,Q. and Weinberger,P.M. (2020) R-loop physiology and pathology: a brief review. *DNA Cell Biol.*, **39**, 1914–1925.
4. Marabitti,V., Valenzisi,P., Lillo,G., Malacaria,E., Palermo,V., Pichierri,P. and Franchitto,A. (2022) R-loop-associated genomic instability and implication of WRN and WRNIP1. *Int. J. Mol. Sci.*, **23**, 1547.
5. Castillo-Guzman,D. and Chedin,F. (2021) Defining R-loop classes and their contributions to genome instability. *DNA Repair (Amst.)*, **106**, 103182.
6. Marnef,A. and Legube,G. (2021) R-loops as Janus-faced modulators of DNA repair. *Nat. Cell Biol.*, **23**, 305–313.
7. Allison,D.F. and Wang,G.G. (2019) R-loops: formation, function, and relevance to cell stress. *Cell Stress*, **3**, 38–46.
8. Abakir,A., Giles,T.C., Cristini,A., Foster,J.M., Dai,N., Starczak,M., Rubio-Roldan,A., Li,M., Eleftheriou,M., Crutchley,J. *et al.* (2020) N(6)-methyladenosine regulates the stability of RNA:DNA hybrids in human cells. *Nat. Genet.*, **52**, 48–55.
9. Cerritelli,S.M. and Crouch,R.J. (2009) Ribonuclease H: the enzymes in eukaryotes. *FEBS J.*, **276**, 1494–1505.
10. Cerritelli,S.M., Sakhuja,K. and Crouch,R.J. (2022) RNase H1, the Gold Standard for R-Loop Detection. *Methods Mol. Biol.*, **2528**, 91–114.
11. Roosen-Runge,E.C. (1962) The process of spermatogenesis in mammals. *Biol. Rev. Camb. Philos. Soc.*, **37**, 343–377.
12. Hess,R.A. and Franca,R., L. (2008) Spermatogenesis and cycle of the seminiferous epithelium. *Adv. Exp. Med. Biol.*, **636**, 1–15.
13. Rathke,C., Baarends,W.M., Awe,S. and Renkawitz-Pohl,R. (2014) Chromatin dynamics during spermiogenesis. *Biochim. Biophys. Acta*, **1839**, 155–168.
14. Bao,J. and Bedford,M.T. (2016) Epigenetic regulation of the histone-to-protamine transition during spermiogenesis. *Reproduction*, **151**, R55–R70.
15. Govin,J., Caron,C., Lestrat,C., Rousseaux,S. and Khochbin,S. (2004) The role of histones in chromatin remodelling during mammalian spermiogenesis. *Eur. J. Biochem.*, **271**, 3459–3469.
16. Jiao,S.Y., Yang,Y.H. and Chen,S.R. (2021) Molecular genetics of infertility: loss-of-function mutations in humans and corresponding knockout/mutated mice. *Hum. Reprod. Update*, **27**, 154–189.
17. Hicks,T., Koury,E., McCabe,C., Williams,C., Crahan,C. and Smolikove,S. (2022) R-loop-induced irreparable DNA damage evades checkpoint detection in the C. elegans germline. *Nucleic Acids Res.*, **50**, 8041–8059.
18. Becherel,O.J., Yeo,A.J., Stellati,A., Heng,E.Y., Luff,J., Suraweera,A.M., Woods,R., Fleming,J., Carrie,D., McKinney,K. *et al.* (2013) Senataxin plays an essential role with DNA damage response proteins in meiotic recombination and gene silencing. *PLoS Genet.*, **9**, e1003435.
19. Yeo,A.J., Becherel,O.J., Luff,J.E., Graham,M.E., Richard,D. and Lavin,M.F. (2015) Senataxin controls meiotic silencing through ATR activation and chromatin remodeling. *Cell Discov.*, **1**, 15025.
20. Becherel,O.J., Fogel,B.L., Zeitlin,S.I., Samaratunga,H., Greaney,J., Homer,H. and Lavin,M.F. (2019) Disruption of spermatogenesis and infertility in ataxia with oculomotor apraxia type 2 (AOA2). *Cerebellum*, **18**, 448–456.
21. Catford,S.R., O'Bryan,M.K., McLachlan,R.I., Delatycki,M.B. and Rombauts,L. (2019) Germ cell arrest associated with aSETX mutation in ataxia oculomotor apraxia type 2. *Reprod. Biomed. Online*, **38**, 961–965.
22. Lin,Z., Hsu,P.J., Xing,X., Fang,J., Lu,Z., Zou,Q., Zhang,K.J., Zhang,X., Zhou,Y., Zhang,T. *et al.* (2017) Mettl3-/Mettl14-mediated mRNA N(6)-methyladenosine modulates murine spermatogenesis. *Cell Res.*, **27**, 1216–1230.
23. Shang,Y., Huang,T., Liu,H., Liu,Y., Liang,H., Yu,X., Li,M., Zhai,B., Yang,X., Wei,Y. *et al.* (2020) MEIOK21: a new component of meiotic recombination bridges required for spermatogenesis. *Nucleic Acids Res.*, **48**, 6624–6639.
24. Luo,M., Yang,F., Leu,N.A., Landaiche,J., Handel,M.A., Benavente,R., La Salle,S. and Wang,P.J. (2013) MEIOB exhibits single-stranded DNA-binding and exonuclease activities and is essential for meiotic recombination. *Nat. Commun.*, **4**, 2788.
25. Zhu,F., Liu,C., Wang,F., Yang,X., Zhang,J., Wu,H., Zhang,Z., He,X., Zhang,Z., Zhou,P. *et al.* (2018) Mutations in PMFBP1 cause acephalic spermatozoa syndrome. *Am. J. Hum. Genet.*, **103**, 188–199.
26. Ahmed,E.A. and de Rooij,D.G. (2009) Staging of mouse seminiferous tubule cross-sections. *Methods Mol. Biol.*, **558**, 263–277.
27. Xu,Z., Song,Z., Li,G., Tu,H., Liu,W., Liu,Y., Wang,P., Wang,Y., Cui,X., Liu,C. *et al.* (2016) H2B ubiquitination regulates meiotic recombination by promoting chromatin relaxation. *Nucleic Acids Res.*, **44**, 9681–9697.
28. Wang,L., Tu,Z., Liu,C., Liu,H., Kaldis,P., Chen,Z. and Li,W. (2018) Dual roles of TRF1 in tethering telomeres to the nuclear envelope and protecting them from fusion during meiosis. *Cell Death Differ.*, **25**, 1174–1188.
29. Misic,J., Milenkovic,D., Al-Behadili,A., Xie,X., Jiang,M., Jiang,S., Filograna,R., Koolmeister,C., Siira,S.J., Jenninger,L. *et al.* (2022) Mammalian RNase H1 directs RNA primer formation for mtDNA replication initiation and is also necessary for mtDNA replication completion. *Nucleic Acids Res.*, **50**, 8749–8766.
30. Lima,W.F., Murray,H.M., Damle,S.S., Hart,C.E., Hung,G., De Hoyos,C.L., Liang,X.H. and Crooke,S.T. (2016) Viable RNaseH1 knockout mice show RNaseH1 is essential for R loop processing, mitochondrial and liver function. *Nucleic Acids Res.*, **44**, 5299–5312.
31. Huh,J.Y., Reilly,S.M., Abu-Odeh,M., Murphy,A.N., Mahata,S.K., Zhang,J., Cho,Y., Seo,J.B., Hung,C.W., Green,C.R. *et al.* (2020) TANK-binding kinase 1 regulates the localization of acyl-CoA synthetase ACSL1 to control hepatic fatty acid oxidation. *Cell Metab.*, **32**, 1012–1027.
32. Zhang,Y., Liu,C., Wu,B., Li,L., Li,W. and Yuan,L. (2021) The missing linker between SUN5 and PMFBP1 in sperm head-tail coupling apparatus. *Nat. Commun.*, **12**, 4926.
33. Modesti,M., Ristic,D., van der Heijden,T., Dekker,C., van Mameren,J., Peterman,E.J., Wuite,G.J., Kanaar,R. and Wyman,C. (2007) Fluorescent human RAD51 reveals multiple nucleation sites and filament segments tightly associated along a single DNA molecule. *Structure*, **15**, 599–609.
34. Modesti,M. (2018) Fluorescent labeling of proteins. *Methods Mol. Biol.*, **1665**, 115–134.
35. Martinez,J.S., von Nicolai,C., Kim,T., Ehlen,A., Mazin,A.V., Kowalczykowski,S.C. and Carreira,A. (2016) BRCA2 regulates DMC1-mediated recombination through the BRC repeats. *Proc. Natl. Acad. Sci. U.S.A.*, **113**, 3515–3520.
36. Luo,S.C., Yeh,H.Y., Lan,W.H., Wu,Y.M., Yang,C.H., Chang,H.Y., Su,G.C., Lee,C.Y., Wu,W.J., Li,H.W. *et al.* (2021) Identification of fidelity-governing factors in human recombinases DMC1 and RAD51 from cryo-EM structures. *Nat. Commun.*, **12**, 115.

37. Yang,Y.J., Song,L., Zhao,X.C., Zhang,C., Wu,W.Q., You,H.J., Fu,H., Zhou,E.C. and Zhang,X.H. (2019) A universal assay for making DNA, RNA, and RNA-DNA hybrid configurations for single-molecule manipulation in two or three steps without ligation. *ACS Synth Biol*, **8**, 1663–1672.

38. Qin,Z.H., Bi,L.L., Hou,X.M., Zhang,S.Q., Zhang,X., Lu,Y., Li,M., Modesti,M., Xi,X.G. and Sun,B. (2020) Human RPA activates BLM's bidirectional DNA unwinding from a nick. *Elife*, **9**, e54098.

39. Bi,L., Qin,Z., Wang,T., Li,Y., Jia,X., Zhang,X., Hou,X.M., Modesti,M., Xi,X.G. and Sun,B. (2022) The convergence of head-on DNA unwinding forks induces helicase oligomerization and activity transition. *Proc. Natl. Acad. Sci. U.S.A.*, **119**, e2116462119.

40. Cerritelli,S.M., Frolova,E.G., Feng,C., Grinberg,A., Love,P.E. and Crouch,R.J. (2003) Failure to produce mitochondrial DNA results in embryonic lethality in Rnaseh1 null mice. *Mol. Cell*, **11**, 807–815.

41. Sadate-Ngatchou,P.I., Payne,C.J., Dearth,A.T. and Braun,R.E. (2008) Cre recombinase activity specific to postnatal, premeiotic male germ cells in transgenic mice. *Genesis*, **46**, 738–742.

42. Lord,T. and Nixon,B. (2020) Metabolic changes accompanying spermatogonial stem cell differentiation. *Dev. Cell*, **52**, 399–411.

43. Zhou,Q., Nie,R., Li,Y., Friel,P., Mitchell,D., Hess,R.A., Small,C. and Griswold,M.D. (2008) Expression of stimulated by retinoic acid gene 8 (Stra8) in spermatogenic cells induced by retinoic acid: an in vivo study in vitamin A-sufficient postnatal murine testes. *Biol. Reprod.*, **79**, 35–42.

44. Bellve,A.R., Cavicchia,J.C., Millette,C.F., O'Brien,D.A., Bhatnagar,Y.M. and Dym,M. (1977) Spermatogenic cells of the prepuberal mouse. Isolation and morphological characterization. *J. Cell Biol.*, **74**, 68–85.

45. Zickler,D. and Kleckner,N. (1999) Meiotic chromosomes: integrating structure and function. *Annu. Rev. Genet.*, **33**, 603–754.

46. Cohen,P.E., Pollack,S.E. and Pollard,J.W. (2006) Genetic analysis of chromosome pairing, recombination, and cell cycle control during first meiotic prophase in mammals. *Endocr. Rev.*, **27**, 398–426.

47. Mahadevaiah,S.K., Turner,J.M., Baudat,F., Rogakou,E.P., de Boer,P., Blanco-Rodriguez,J., Jasin,M., Keeney,S., Bonner,W.M. and Burgoyne,P.S. (2001) Recombinational DNA double-strand breaks in mice precede synapsis. *Nat. Genet.*, **27**, 271–276.

48. Gray,S. and Cohen,P.E. (2016) Control of meiotic crossovers: from double-strand break formation to designation. *Annu. Rev. Genet.*, **50**, 175–210.

49. Anderson,L.K., Reeves,A., Webb,L.M. and Ashley,T. (1999) Distribution of crossing over on mouse synaptonemal complexes using immunofluorescent localization of MLH1 protein. *Genetics*, **151**, 1569–1579.

50. Lange,J., Pan,J., Cole,F., Thelen,M.P., Jasin,M. and Keeney,S. (2011) ATM controls meiotic double-strand-break formation. *Nature*, **479**, 237–240.

51. Uziel,T., Lerenthal,Y., Moyal,L., Andegeko,Y., Mittelman,L. and Shiloh,Y. (2003) Requirement of the MRN complex for ATM activation by DNA damage. *EMBO J.*, **22**, 5612–5621.

52. Lukaszewicz,A., Lange,J., Keeney,S. and Jasin,M. (2018) Control of meiotic double-strand-break formation by ATM: local and global views. *Cell Cycle*, **17**, 1155–1172.

53. Ribeiro,J., Dupaigne,P., Petrillo,C., Ducrot,C., Duquenne,C., Veaute,X., Saintome,C., Busso,D., Guerois,R., Martini,E. *et al.* (2021) The meiosis-specific MEIOB-SPATA22 complex cooperates with RPA to form a compacted mixed MEIOB/SPATA22/RPA/ssDNA complex. *DNA Repair (Amst.)*, **102**, 103097.

54. Souquet,B., Abby,E., Herve,R., Finsterbusch,F., Tourpin,S., Le Bouffant,R., Duquenne,C., Messiaen,S., Martini,E., Bernardino-Sgherri,J. *et al.* (2013) MEIOB targets single-strand DNA and is necessary for meiotic recombination. *PLoS Genet.*, **9**, e1003784.

55. Zhang,J., Fujiwara,Y., Yamamoto,S. and Shibuya,H. (2019) A meiosis-specific BRCA2 binding protein recruits recombinases to DNA double-strand breaks to ensure homologous recombination. *Nat. Commun.*, **10**, 722.

56. Zhang,J., Gurusaran,M., Fujiwara,Y., Zhang,K., Echbarthi,M., Vorontsov,E., Guo,R., Pendlebury,D.F., Alam,I., Livera,G. *et al.* (2020) The BRCA2-MEILB2-BRME1 complex governs meiotic recombination and impairs the mitotic BRCA2-RAD51 function in cancer cells. *Nat. Commun.*, **11**, 2055.

57. Zhang,J., Nandakumar,J. and Shibuya,H. BRCA2 in mammalian meiosis. (2022) *Trends Cell Biol.*, **32**, 281–284.

58. Mhaskar,A.N., Koornneef,L., Zelensky,A.N., Houtsmuller,A.B. and Baarends,W.M. (2021) High resolution view on the regulation of recombinase accumulation in mammalian meiosis. *Front. Cell Dev. Biol.*, **9**, 672191.

59. Cloud,V., Chan,Y.L., Grubb,J., Budke,B. and Bishop,D.K. (2012) Rad51 is an accessory factor for Dmc1-mediated joint molecule formation during meiosis. *Science*, **337**, 1222–1225.

60. Prakash,R., Sandoval,T., Morati,F., Zagelbaum,J.A., Lim,P.X., White,T., Taylor,B., Wang,R., Desclos,E.C.B., Sullivan,M.R. *et al.* (2021) Distinct pathways of homologous recombination controlled by the SWS1-SWSAP1-SPIDR complex. *Nat. Commun.*, **12**, 4255.

61. Pazhayam,N.M., Turcotte,C.A. and Sekelsky,J. (2021) Meiotic crossover patterning. *Front. Cell Dev. Biol.*, **9**, 681123.

62. Qiao,H., Prasada Rao,H.B., Yang,Y., Fong,J.H., Cloutier,J.M., Deacon,D.C., Nagel,K.E., Swartz,R.K., Strong,E., Holloway,J.K. *et al.* (2014) Antagonistic roles of ubiquitin ligase HEI10 and SUMO ligase RNF212 regulate meiotic recombination. *Nat. Genet.*, **46**, 194–199.

63. Tsubouchi,H. and Roeder,G.S. (2003) The importance of genetic recombination for fidelity of chromosome pairing in meiosis. *Dev. Cell*, **5**, 915–925.

64. Petukhova,G.V., Pezza,R.J., Vanevski,F., Ploquin,M., Masson,J.Y. and Camerini-Otero,R.D. (2005) The Hop2 and Mnd1 proteins act in concert with Rad51 and Dmc1 in meiotic recombination. *Nat. Struct. Mol. Biol.*, **12**, 449–453.

65. Phillips,D.D., Garboczi,D.N., Singh,K., Hu,Z.L., Leppla,S.H. and Leysath,C.E. (2013) The sub-nanomolar binding of DNA–RNA hybrids by the single-chain Fv fragment of antibody S9.6. *J. Mol. Recognit.*, **26**, 376–381.

66. Liu,S., Hua,Y., Wang,J., Li,L., Yuan,J., Zhang,B., Wang,Z., Ji,J. and Kong,D. (2021) RNA polymerase III is required for the repair of DNA double-strand breaks by homologous recombination. *Cell*, **184**, 1314–1329.

67. Wang,T., Hu,J.J., Li,Y.A., Bi,L.L., Guo,L.J., Jia,X.S., Zhang,X., Li,D., Hou,X.M., Modesti,M. *et al.* (2022) Bloom syndrome helicase compresses single-stranded DNA into phase-separated condensates. *Angew Chem Int Edit*, **61**, e202209463.

68. Zhang,C., Fu,H., Yang,Y., Zhou,E., Tan,Z., You,H. and Zhang,X. (2019) The mechanical properties of RNA-DNA hybrid duplex stretched by magnetic tweezers. *Biophys. J.*, **116**, 196–204.

69. Keeney,S., Lange,J. and Mohibullah,N. (2014) Self-organization of meiotic recombination initiation: general principles and molecular pathways. *Annu. Rev. Genet.*, **48**, 187–214.

70. Lam,I. and Keeney,S. (2014) Mechanism and regulation of meiotic recombination initiation. *Cold Spring Harb. Perspect. Biol.*, **7**, a016634.

71. Yadav,V.K. and Claeys Bouuaert,C. (2021) Mechanism and control of meiotic DNA double-strand break formation in *S. cerevisiae*. *Front. Cell Dev. Biol.*, **9**, 642737.

72. Brickner,J.R., Garzon,J.L. and Cimprich,K.A. (2022) Walking a tightrope: the complex balancing act of R-loops in genome stability. *Mol. Cell*, **82**, 2267–2297.

73. Ohle,C., Tesorero,R., Schermann,G., Dobrev,N., Sinning,I. and Fischer,T. (2016) Transient RNA-DNA hybrids are required for efficient double-strand break repair. *Cell*, **167**, 1001–1013.

74. Yasuhara,T., Kato,R., Hagiwara,Y., Shiotani,B., Yamauchi,M., Nakada,S., Shibata,A. and Miyagawa,K. (2018) Human Rad52 promotes XPG-mediated R-loop processing to initiate transcription-associated homologous recombination repair. *Cell*, **175**, 558–570.

75. Keskin,H., Shen,Y., Huang,F., Patel,M., Yang,T., Ashley,K., Mazin,A.V. and Storici,F. (2014) Transcript-RNA-templated DNA recombination and repair. *Nature*, **515**, 436–439.

76. Zhang,C., Chen,L., Peng,D., Jiang,A., He,Y., Zeng,Y., Xie,C., Zhou,H., Luo,X., Liu,H. *et al.* (2020) METTL3 and N6-methyladenosine promote homologous recombination-mediated repair of DSBs by modulating DNA–RNA hybrid accumulation. *Mol. Cell*, **79**, 425–442.

77. Ouyang,J., Yadav,T., Zhang,J.M., Yang,H., Rheinbay,E., Guo,H., Haber,D.A., Lan,L. and Zou,L. (2021) RNA transcripts stimulate homologous recombination by forming DR-loops. *Nature*, **594**, 283–288.

78. Brown,M.S. and Bishop,D.K. (2014) DNA strand exchange and RecA homologs in meiosis. *Cold Spring Harb. Perspect. Biol.*, **7**, a016659.

79. Crickard,J.B. and Greene,E.C. (2018) Biochemical attributes of mitotic and meiotic presynaptic complexes. *DNA Repair (Amst.)*, **71**, 148–157.

80. Xu,J., Zhao,L., Peng,S., Chu,H., Liang,R., Tian,M., Connell,P.P., Li,G., Chen,C. and Wang,H.W. (2021) Mechanisms of distinctive mismatch tolerance between Rad51 and Dmc1 in homologous recombination. *Nucleic Acids Res.*, **49**, 13135–13149.

81. Hinch,A.G., Becker,P.W., Li,T., Moralli,D., Zhang,G., Bycroft,C., Green,C., Keeney,S., Shi,Q., Davies,B. *et al.* (2020) The configuration of RPA, RAD51, and DMC1 binding in meiosis reveals the nature of critical recombination intermediates. *Mol. Cell*, **79**, 689–701.

82. Yang,X., Zhai,B., Wang,S., Kong,X., Tan,Y., Liu,L., Yang,X., Tan,T., Zhang,S. and Zhang,L. (2021) RNA-DNA hybrids regulate meiotic recombination. *Cell Rep.*, **37**, 110097.

83. Domingo-Prim,J., Endara-Coll,M., Bonath,F., Jimeno,S., Prados-Carvajal,R., Friedlander,M.R., Huertas,P. and Visa,N. (2019) EXOSC10 is required for RPA assembly and controlled DNA end resection at DNA double-strand breaks. *Nat. Commun.*, **10**, 2135.

84. Yang,Y., Xu,W., Gao,F., Wen,C., Zhao,S., Yu,Y., Jiao,W., Mi,X., Qin,Y., Chen,Z.J. *et al.* (2022) Transcription-replication conflicts in primordial germ cells necessitate the Fanconi anemia pathway to safeguard genome stability. *Proc. Natl. Acad. Sci. U.S.A.*, **119**, e2203208119.